Master's thesis

Anomalous couplings of the top quark

Asbjørn Sørensen Bols

Advisor: Jørgen Beck Hansen

Submitted: May 22, 2023

Abstract

The top quark, as the most massive of all observed elementary particles, has the exclusive advantage of being the optimal candidate to reveal the mystery of physics beyond the Standard Model of particle physics (BSM). Anomalous contributions to $t\bar{t}$ production can be investigated in the framework of Standard Model Effective Field Theory (SMEFT). The potential new contributions are expected to affect the production cross section and angular distributions of the top decay products due to changed spin configurations. The Future Circular Collider (FCC) process $e^+e^- \rightarrow t\bar{t}$ will be simulated using the IDEA detector setup and investigated with the aim to gauge the potential experimental sensitivity to anomalous top contributions. The project will focus on all decay configurations of a $t\bar{t}$ system, which is expected to be possible in the very clean conditions of e^+e^- colliders. Event selection is used to select the collision events of interest with respect to background and apply a kinematic reconstruction to determine the complete kinematic configuration of each event. This allows to determine the production cross section and investigate potential observables (production & decay angles and optimal observables a.o.) for their sensitivity to BSM contributions. The final goal is to fit the anomalous gauge coupling parameters using both the kinematical observables and cross section information.

Contents

Introduction

Since ancient times, the human race has sought understanding of the fundamental principles that control nature. It was once believed that everything consisted of four elements: earth, wind, fire and water. We now know that the "elements" are more complicated than that. Elementary particle physics is the study of the fundamental constituents of matter, the elementary particles, and the forces that act between them. The goal of particle physics is to discover the unifying principles of the universe use them to form a complete picture of physics.

Great effort have been made in unifying the four forces of nature. The electromagnetic and weak forces were combined in a consistent theory today known as the *electroweak* theory. *Quantum Chromodynamics* (QCD), the theory behind the strong force, was combined with the electroweak theory to create the *Standard Model*. The Standard Model is based on a underlying symmetry called *local gauge invariance* and a neutral particle, *the Higgs boson*. In 2012 the Higgs boson was discovered at the Large Hadron Collider (LHC) [1] and verified the most important predictions of the Standard Model.

The Standard Model is not a complete theory, however. It cannot give a fully predictive model for the gravitational force and fails to encompass phenomena such as non-baryonic dark matter, neutrino masses and the cosmological baryon-antibaryon asymmetry. This leads particle physicists to look for phenomena beyond the predictions of the Standard Model. One place to begin the search is with the top quark. The top quark is the heaviest particle in the Standard Model with a mass around 173 GeV [2] and is comparable with the Higgs expectation value. The high mass of the top quark indicates a stronger coupling to fields outside the Standard Model.

The European Organisation for Nuclear Research (CERN) is the leading frontier within the field of high energy particle physics, owing responsibility for the LHC and the discovery of the Higgs boson. CERNs next project is the Future Circular Collider (FCC), where in the FCC-ee experiment electron positron collisions seek to produce measurements with unprecedented levels of precision. With higher levels of precision, smaller and smaller variations from predictions can be observed.

This thesis seeks to determine the measurement sensitivity of anomalous top quark coupling constants at the FCC-ee. The anomalous coupling constants to the top quark are couplings that do not exist within the Standard Model but can be introduced through supplementing the original framework with Effective Field Theories. By comparing simulations of particle physics at the

FCC-ee with and without anomalous coupling constants, the measurement sensitivity is determined by performing the necessary steps to select and reconstruct top quark collisions.

The section Theoretical Basis gives an overview of gauge invariance and some of the Standard Model relevant to the top quark production experiment. The relevant anomalous coupling constants are introduced and an overview of the the top quark production through electron-positron annihilation is given. The Experimental Apparatus section gives an overview of the experimental conditions planned at the FCC and the IDEA detector. The exact details of the experiment still require finalization and many aspects are prone to change. The framework used to simulate the particle physics and the anomalous physics at the FCC is outlined. This study is performed on the semileptonic decay channel of top pairs produced at a centre-of-mass energy of $\sqrt{s} = 365\,\mathrm{GeV}$. The Event Selection & Reconstruction section outlines the event selection and the considerations made in association with it. The event selection is performed in two parts. In the first part the reconstruction of the event is ensured through manual selection. In the second part machine learning algorithms are used to differentiate between events. Through a kinematic fit the event reconstruction is performed after the event selection. The resulting confidence intervals of the anomalous coupling constants are shown in the Analysis section where the effects of the event selection on the event samples is also studied.

Theoretical basis

Gauge invariance

One of the most profound insights in theoretical physics is that interactions are dictated by principles of symmetry. Analytical mechanics tells us that invariance under translation, time displacement and rotation leads to conservation of momentum, energy and angular momentum, respectively. In a similar vein, the conservation of charge, both electric charge and colour charge, is derived from a different type of invariance under gauge transformation. For a gauge theory, the Lagrangian must be gauge invariant, i.e. it must be invariant under gauge transformations of the particle fields, like the one shown in equation (1).

$$\psi(x) \rightarrow e^{i\alpha}\psi(x) \tag{1}$$

the implication here is that the phase α cannot be measured and can thus be chosen arbitrarily. If α is a fixed as constant across all of space and time, we call equation (1) a *global* gauge transformation. If the phase instead were space and time dependant $\alpha = \alpha(x)$, the equation would be a *local* gauge transformation. A local gauge transformation is a much stronger requirement for gauge theories. The standard model is based on the assumption that gauge theories describes the fundamental forces of the universe, and as we shall see, the electroweak theory is a gauge invariant quantum field theory.

Quantum electrodynamics

Quantum electrodynamics (QED) is the gauge theory that describes electromagnetic interactions and is gauge invariant under the local gauge transformation $U(1)$. QED can be described somewhat simply with Lagrangian formalism by the following equation [3]

$$\mathcal{L}_{QED} = -\frac{1}{4}F_{\mu\nu}F^{\mu\nu} + \overline{\psi}(i\gamma^\mu\partial_\mu - m)\psi - q\overline{\psi}\gamma^\mu\psi A_\mu \tag{2}$$

Where ψ represents the half-spin spinor field of a fermion with charge q and mass m while A_μ represents the photon field. $F_{\mu\nu}$ is the electromagnetic tensor and is dependent only on A_μ, such that the first term describes the free photon, the second term describes free fermions and the last term describes the interaction between fermions and photons. The notation of an upper index with the same symbol as a lower index indicates a sum over all indices, such that $a^\mu b_\mu = \sum_{\mu=0}^{4}\sum_{\nu=0}^{4} g_{\mu\nu}a_\mu b_\nu$ and $p^\mu p_\mu = E^2 - |\vec{p}|^2 = m^2$. The γ^μ are

the gamma matrices and we will often abbreviate them with slash notation $\gamma^\mu a_\mu = \slashed{a}$. Using the Euler-Lagrange equation on the second term of equation (2) with respect to $\overline{\psi}$, we see that the Lagrangian satisfies the Dirac equation [3]

$$i\slashed{\partial}\psi - m\psi = 0 \tag{3}$$

Equation (2) also needs to satisfy local $U(1)$ gauge symmetry, which means that the Lagrangian must be invariant under transformations of the fields. The spinor field and the photon field transforms as

$$\psi(x) \rightarrow e^{i\alpha(x)}\psi(x) \tag{4}$$

$$A_\mu(x) \rightarrow A_\mu(x) + \partial_\mu\alpha(x) \tag{5}$$

In order for the Lagrangian to satisfy these transformations we need to replace the partial derivatives ∂_μ with the covariant derivative D_μ

$$\partial_\mu \rightarrow D_\mu = \partial_\mu + iqA_\mu \tag{6}$$

This leads to the Lagrangian to take the form

$$\mathcal{L}_{QED} = -\frac{1}{4}F_{\mu\nu}F^{\mu\nu} + \overline{\psi}(i\slashed{D} - m)\psi - q\overline{\psi}\slashed{A}\psi \tag{7}$$

In the same manner this technique can be applied to other symmetry groups to derive lagrangians for the weak and strong interactions by requiring a local $SU(2)$ gauge symmetry and $SU(3)$ gauge symmetry, respectively, for a lagrangian that satisfies the Dirac equation. This study will omit an explanation of the strong interaction and instead focus on the unification of QED with weak interactions.

The Standard model

The Standard Model of Particle Physics (SM) is the theory that postulates that all matter is made up of point-like spin-half particles known as *fermions*, and that the interactions between these fermions is dictated by the force carrying *bosons*. The fermions are spin $\frac{1}{2}$ particles divided into leptons and quarks, where the distinction is that the quarks interacts with the strong force. Each fermion has an anti-particle with equal and opposite quantum numbers, while the bosons are their own anti-particles. The gauge bosons are spin 1 particles and are responsible for the electromagnetic force, which mediated by the photon, the weak force, which is mediated by the W and Z bosons, and the strong force which is mediated by the gluons. Additionally, the Higgs boson is a scalar particle with spin 0, which is required in order for
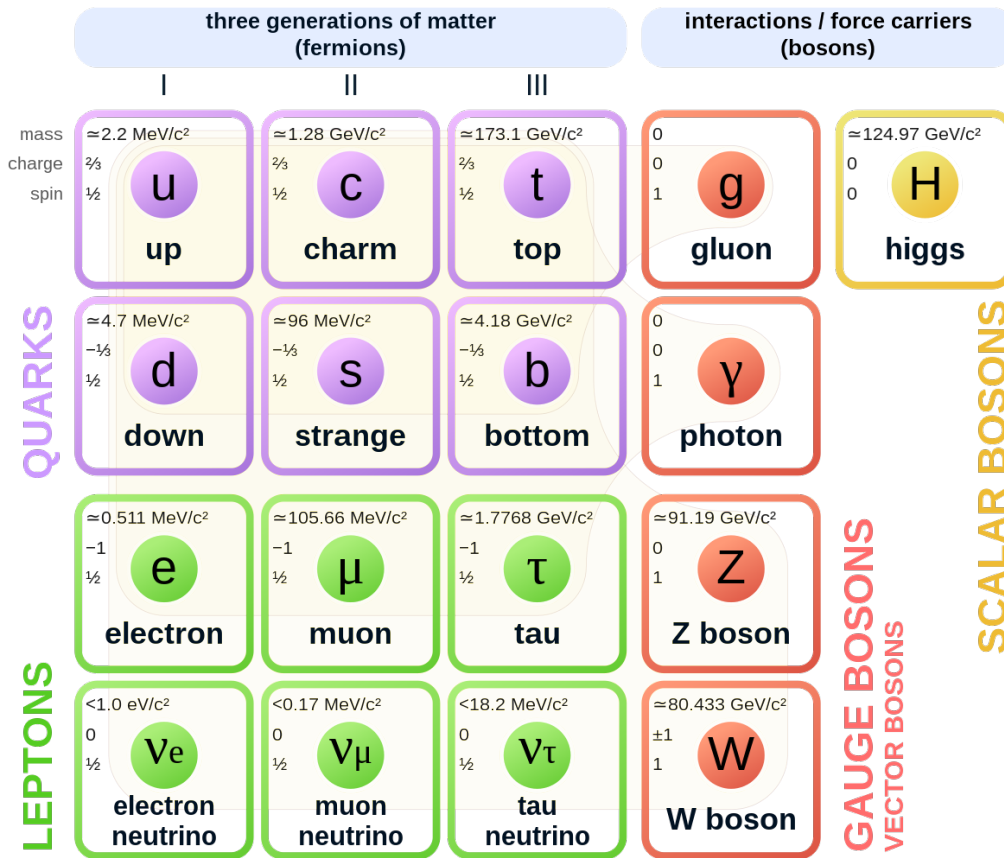
Standard Model of Elementary Particles

	three generations of matter (fermions)			interactions / force carriers (bosons)	

QUARKS

	I	II	III		
mass charge spin	≃2.2 MeV/c² ⅔ ½ **u** **up**	≃1.28 GeV/c² ⅔ ½ **c** **charm**	≃173.1 GeV/c² ⅔ ½ **t** **top**	0 0 1 **g** **gluon**	≃124.97 GeV/c² 0 0 **H** **higgs**
	≃4.7 MeV/c² −⅓ ½ **d** **down**	≃96 MeV/c² −⅓ ½ **s** **strange**	≃4.18 GeV/c² −⅓ ½ **b** **bottom**	0 0 1 **γ** **photon**	

LEPTONS

	≃0.511 MeV/c² −1 ½ **e** **electron**	≃105.66 MeV/c² −1 ½ **μ** **muon**	≃1.7768 GeV/c² −1 ½ **τ** **tau**	≃91.19 GeV/c² 0 1 **Z** **Z boson**	
	<1.0 eV/c² 0 ½ **νe** **electron neutrino**	<0.17 MeV/c² 0 ½ **νμ** **muon neutrino**	<18.2 MeV/c² 0 ½ **ντ** **tau neutrino**	≃80.433 GeV/c² ±1 1 **W** **W boson**	

GAUGE BOSONS / VECTOR BOSONS

SCALAR BOSONS

Figure 1: The Standard Model of Particle Physics. Each of the 17 particles that SM predicts is displayed. The fermions are displayed in the first three columns, the gauge bosons in the fourth column and the higgs boson in the final column. The fermions are divided into three generations, one for each column. Each generation has a quark with electric charge $+\frac{2}{3}$, a quark with electric charge $-\frac{1}{3}$, a negatively charged lepton and a corresponding neutrino with no charge.
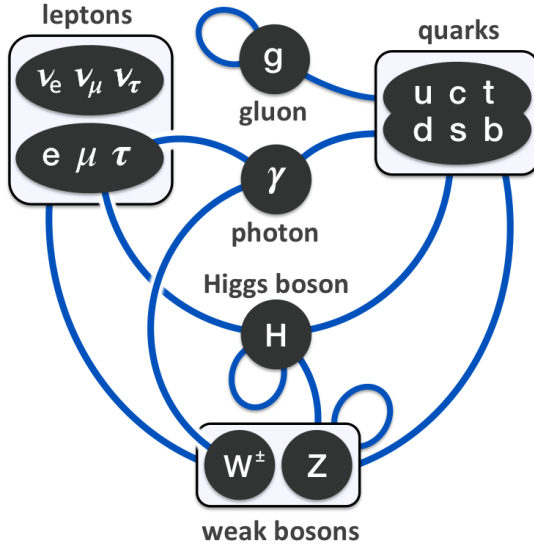
Figure 2: The allowed interactions of the Standard Model. The electrically charged particles interact with the photon, the quarks interact with the gluon, the Higgs interacts with particles wiht mass, and the weak bosons are the only particles that interact with neutrinos.

the W and Z bosons to have mass. It is believed that the Higgs mechanism is also responsible for giving the fermions their masses.

The electrically charged particles interact with the photons, the quarks interact with the gluons and every fermion interacts with the W and Z bosons. Additionally, the bosons can interact with each other. Gluons can self-interact, photons can interact with W bosons and the weak bosons can interact with each other. There is also the Higgs boson which is a scalar boson with spin 0 where the particles have mass because of their interaction with the Higgs field, as such the Higgs boson interacts with all particles with mass, including itself. A diagram of which particles interact with which is shown in Figure 2. The standard model is not a complete theory of fundamental interactions, however, since it does not fully incorporate gravity and baryon asymmetry. The Standard Model is based on the gauge group

$$SU(3)_C \times SU(2)_L \times U(1)_Y \tag{8}$$

where the $SU(3)_C$ represent the gauge group of Quantum Chromodynamics (QCD) with color charge C, $SU(2)_L \times U(1)_Y$ represents the gauge group of the electroweak interactions, with L and Y representing the weak isospin and weak hypercharge, respectively.

Electroweak unification

Electroweak is a gauge theory based on the $SU(2) \times U(1)$ group and has four gauge fields, the photon, the Z boson and the $W^{\pm}$ bosons. In the 1960s, Glashow, Salam and Weinberg (GSW) developed a unified picture of the electromagnetic and weak interactions. One consequence of the GSW model is the prediction of a weak neutral-current mediated by the neutral Z boson [3]. The charged-current weak interaction is associated with $SU(2)$ local gauge symmetries. The generators for $SU(2)$ can be written in terms of the three 2×2 Pauli spin matrices, requiring three gauge fields corresponding to three gauge bosons, $W^{(1)}$, $W^{(2)}$ and $W^{(3)}$, to satisfy the local gauge invariance. The wavefunction is described as weak isospin doublets, since they are required to have two components to satisfy the dimensions of the Pauli matrices. Particle states can either have left-handed or right-handed chirality. Chirality does not have any simple physical interpretation, but is related to the helicity combinations that give non-zero matrix elements, where helicity is the spin projection onto the movement direction of a particle. The weak charged bosons only couple to left-handed chiral particle states and and right-handed chiral antiparticle states, which corresponds to $SU(2)$ doublets and singlets, with weak isospin $I_W = \frac{1}{2}$ and $I_W = 0$, respectively.

$$\begin{pmatrix} \nu_e \\ e^- \end{pmatrix}_L, \quad \begin{pmatrix} \nu_\mu \\ \mu^- \end{pmatrix}_L, \quad \begin{pmatrix} \nu_\tau \\ \tau^- \end{pmatrix}_L, \quad \begin{pmatrix} u \\ d' \end{pmatrix}_L, \quad \begin{pmatrix} c \\ s' \end{pmatrix}_L, \quad \begin{pmatrix} t \\ b' \end{pmatrix}_L \tag{9}$$

$$e_R^-, \quad \mu_R^-, \quad \tau_R^-, \quad u_R, \quad c_R, \quad t_R, \quad d_R, \quad s_R, \quad b_R \tag{10}$$

The weak isospin doublets are given in (9) and the weak isospin singlets are given in (10). Since the singlets are unaffected by the $SU(2)$ local gauge transformation, they do not couple to the gauge bosons. The physical W bosons can be identified as a linear combination of $W^{(1)}$ and $W^{(2)}$

$$W^{\pm} = \frac{1}{\sqrt{2}}(W^{(1)} \mp iW^{(2)}) \tag{11}$$

Since the gauge bosons only couple to left-handed particles and right-handed antiparticles, we expect the Z boson to do the same. However, experimentation shows that Z bosons couple to both left-handed and right-handed particles. From this came the idea that the photons and Z bosons, with corresponding fields A_μ and Z_μ, each come from a mixing of the $U(1)$ gauge field B_μ and the neutral $SU(2)$ field $W_\mu^{(3)}$

$$A_\mu = +B_\mu \cos\theta_W + W_\mu^{(3)} \sin\theta_W \tag{12}$$

$$Z_\mu = -B_\mu \cos\theta_W + W_\mu^{(3)} \sin\theta_W \tag{13}$$

where θ_W is the weak mixing angle. The B_μ field couples to a new kind of charge, termed weak hypercharge Y, which causes the electromagnetic charge to be derived from the more fundamental weak hypercharge and weak isospin

$$Q = \frac{Y}{2} + I_W^{(3)} \tag{14}$$

where Q is the electric charge and $I_W^{(3)}$ is the third component of the weak isospin. The weak mixing angle θ_W relates the weak bosons and the photon through their coupling terms

$$e = g_W \sin\theta_W = g_Z \sin\theta_W \cos\theta_W = g' \cos\theta_W \tag{15}$$

where e is the electric charge of an electron, g_W is the coupling strength of the $W^\pm$ bosons, g_Z is the coupling strength of the Z boson and g' is the coupling strength of the B_μ field. With this electroweak unification, the Z boson can now couple to both the left-handed and right-handed chiral states, though with different coupling strengths, which are given by

$$c_L = I_W^{(3)} - Q\sin^2\theta_W, \quad c_R = -Q\sin^2\theta_W \tag{16}$$

with c_L being the coupling to left-handed states and c_R being the coupling to right-handed states. By requiring the Lagrangian for the electroweak theory be invariant under $U(1)$ and $SU(2)$ local gauge transformations, we get the covariant derivative for the $U(1)_Y \times SU(2)_L$ group

$$\partial_\mu \rightarrow D_\mu = \partial_\mu + ig_W \mathbf{T} \cdot \mathbf{W}_\mu(x) + ig'\frac{Y}{2}B_\mu \tag{17}$$

where $\mathbf{T} = \frac{\boldsymbol{\sigma}}{2}$ are the three generators of $SU(2)$, $\mathbf{W}_\mu$ is the vector of gauge fields W_μ of $SU(2)$ and B_μ is the $U(1)_Y$ gauge field with hypercharge Y. This covariant derivative ensures that the Lagrangian is invariant under $U(1)_Y \times SU(2)_L$ local gauge transformations, such that the electroweak Lagrangian becomes a valid. Thus we have shown that the $U(1)$ QED gauge theory and the $SU(2)$ weak interaction gauge theory can be unified into one $U(1)_Y \times SU(2)_L$ electroweak gauge theory. We need one more element however, since local gauge symmetry of (17) requires that the bosons are massless, and does not account for the B_μ field. This local gauge symmetry breaking is a problem that can only be mitigated through the introduction of the Higgs mechanism.
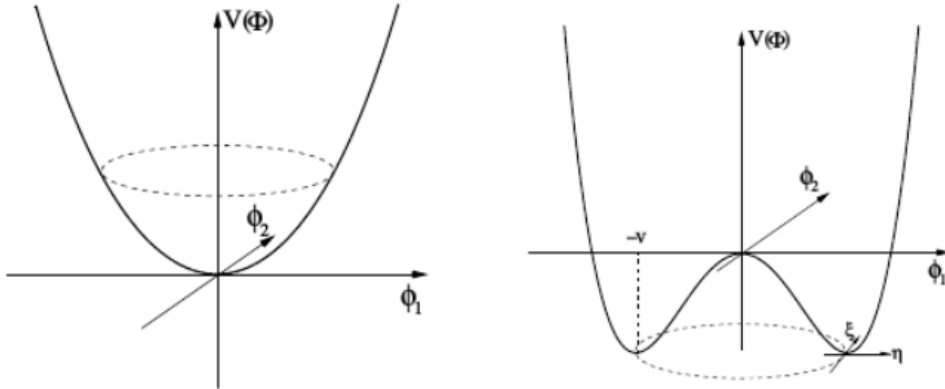
Figure 3: The Higgs potential. On the left with $\mu^2 > 0$. On the right with $\mu^2 < 0$.

Higgs

The Higgs mechanism and the associated Higgs boson are essential parts of the Standard Model. The Higgs mechanism is the way that the W and Z bosons acquire mass without breaking the local gauge symmetry of the Standard Model [3]. Since the gluon and the photon are massless, there was no breaking of local gauge symmetry in QED and QCD, but since the weak bosons do have mass, introducing mass via the Higgs mechanism makes once again makes the theory renormalizable. In the Salam-Weinberg theory, the Higgs mechanism is embedded in the $U(1)_Y \times SU(2)_L$ local gauge symmetry. Because the Higgs mechanism is required to generate masses of the electroweak gauge bosons, one of the scalar fields must be neutral and one must be charged. Thus the minimal Higgs model consists of two complex scalar fields, placed in a weak isospin doublet

$$\phi = \begin{pmatrix} \phi^+ \\ \phi^0 \end{pmatrix} = \frac{1}{\sqrt{2}} \begin{pmatrix} \phi_1 + i\phi_2 \\ \phi_3 + i\phi_4 \end{pmatrix} \tag{18}$$

The Lagrangian for this doublet of complex scalar fields is

$$\mathcal{L}_{Higgs} = (D_\mu \phi)^\dagger (D^\mu \phi) - V(\phi) \tag{19}$$

where $V(\phi)$ is the Higgs potential and the covariant derivative D_μ is given by equation (17). The self interaction term of the Higgs field, the potential V, is chosen to be the right potential in Figure (3).

$$V(\phi) = \mu^2 \phi^\dagger \phi + \lambda(\phi^\dagger \phi)^2 \tag{20}$$

9

where $\mu^2 < 0$ and $\lambda > 0$. The potential has an infinite set of degenerate minima satisfying

$$\phi^\dagger \phi = \frac{1}{2}(\phi_1^2 + \phi_2^2 + \phi_3^2 + \phi_4^2) = \frac{v^2}{2} = -\frac{\mu^2}{2\lambda} \tag{21}$$

The Vacuum Expectation Value (VEV) $v = 246\,\text{GeV}$ is the energy of the lowest energy state of the field i.e. the vacuum state. Since the photon is required to remain massless after symmetry breaking, the minimum of the potential must correspond to a non-zero VEV of the neutral scalar field ϕ^0

$$\langle 0|\phi|0\rangle = \frac{1}{\sqrt{2}} \begin{pmatrix} 0 \\ v \end{pmatrix} \tag{22}$$

then we can expand the field about this minimum and perform some suitable gauge transformations to obtain

$$\phi(x) = \frac{1}{\sqrt{2}} \begin{pmatrix} 0 \\ v + h(x) \end{pmatrix} \tag{23}$$

where $h(x)$ is the physical Higgs field. The Lagrangian from equation (19) describe the massive Higgs scalar, the massive and massless gauge bosons, the interactions between the Higgs and the gauge bosons as well as the Higgs self-interaction. This means we can derive the gauge boson masses from the $(D_\mu\phi)^\dagger(D^\mu\phi)$ term and the Higgs mass from the self-interaction term. By substituting for equation (17) and (23) and reducing we get

$$m_H = \sqrt{2\lambda}v \tag{24}$$

$$m_W = \frac{1}{2}g_W v \tag{25}$$

$$m_Z = \frac{1}{2}\sqrt{g_W^2 + g'^2} = \frac{1}{2}\frac{g_W v}{\cos\theta_W} \tag{26}$$

$$m_A = 0 \tag{27}$$

$$m_f = \frac{1}{\sqrt{2}}g_f v \tag{28}$$

where m_H, m_W, m_Z and m_A are the Higgs mass, the $W^\pm$ boson mass, the Z boson mass and the photon mass, respectively. Additionally an equation for the fermion masses m_f can be obtained, using the Yukawa coupling g_f even though this coupling is not necessarily predicted by the Higgs mechanism, but can be chosen to be consistent with the observed fermion masses.

Extending the Standard Model with Effective Field Theories

Imagine a theory for new physics at a high energy scale, Λ. At lower energies the operators that describe the new theory would become almost completely negligible. In such cases it can be more efficient to make an Effective Field Theory (EFT), which instead of describing the full theory simply describes the contribution of the total theory. This is especially useful for describing the effects of the theory without knowing the exact theory. As an example, quantum gravity can be described at low energy scales quite well with an EFT. Since the Standard Model is a consistent but not complete theory, it can be considered an EFT at low energies.

The idea behind EFT is to add an effective Lagrangian to our existing SM Lagrangian that describe higher-order contributions which will become more relevant at higher energy colliders. The SM is a theory based on dimension 4, which is the lowest possible dimension that can be both Lorentz invariant and satisfy the $SU(3)_C \times SU(2)_L \times U(1)_Y$ gauge symmetries of the SM. As such the total Lagrangian for the SM with EFT contributions (SMEFT), can be described by

$$\mathcal{L}_{SMEFT} = \mathcal{L}_{SM} + \sum_i \frac{c_i^{(6)}}{\Lambda^2} O_i^{(6)} + \sum_j \frac{c_j^{(8)}}{\Lambda^4} O_j^{(8)} + \dots \tag{29}$$

where $O_i^{(d)}$ are operators with dimension d, c_i are the coefficients for the operators and Λ is the characteristic length scale, which ensures the coefficients remain dimensionless. Only operators that obey the symmetries of the SM are included. Operators with uneven dimension cannot conserve both baryon number and lepton number. Thus the lowest dimension contribution to the SM Lagrangian is of dimension-6. Higher dimension terms are suppressed by the characteristic energy $\frac{1}{\Lambda^{d-4}}$. For the purpose of this study we choose to neglect contributions of higher orders and simply focus on the dimension 6 operators, since their contributions are larger. A total of 59 independent operators exist at the dimension 6 level [7], however we are only interested in the anomalous top quark behaviour, so we can reduce this number to only those relevant for the top quark decay.

Since we examine electron positron collisions and we choose not to examine flavour changing vertices, the vertices we are interested in are the Wtb, $Zt\bar{t}$ and $\gamma t\bar{t}$ vertices. There are 7 independent operators that contribute to the

Wtb, $Zt\bar{t}$ and $\gamma t\bar{t}$ vertices and in the notation of [8] they are

$$O_{\phi q}^{(3)} = i(\phi^\dagger \tau^I D_\mu \phi)(\bar{q}_L \gamma^\mu \tau^I q_L) \tag{30}$$

$$O_{\phi q}^{(1)} = i(\phi^\dagger D_\mu \phi)(\bar{q}_L \gamma^\mu q_L) \tag{31}$$

$$O_{\phi\phi} = i(\widetilde{\phi}^\dagger D_\mu \phi)(\bar{t}_R \gamma^\mu b_R) \tag{32}$$

$$O_{\phi t} = i(\phi^\dagger D_\mu \phi)(\bar{t}_R \gamma^\mu r_R) \tag{33}$$

$$O_{tW} = (\bar{q}_L \sigma^{\mu\nu} \tau^I t_R)\widetilde{\phi} W_{\mu\nu}^I \tag{34}$$

$$O_{bW} = (\bar{q}_L \sigma^{\mu\nu} \tau^I b_R)\phi W_{\mu\nu}^I \tag{35}$$

$$O_{tB\phi} = (\bar{q}_L \sigma^{\mu\nu} t_R)\widetilde{\phi} B_{\mu\nu} \tag{36}$$

$$\tag{37}$$

with covariant derivative

$$D_\mu = \partial_\mu + ig_s \frac{\lambda^a}{2} G_\mu^a + ig \frac{\tau^I}{2} W_\mu^I + ig' Y B_\mu \tag{38}$$

where G_μ^a, W_μ^I and B_μ are the gauge fields for $SU(3)$, $SU(2)$ and $U(1)$, respectively. λ^a are the Gell-Mann matricies with $a = 1, \ldots 8$, τ^I are the Pauli matrices for $I = 1, 2, 3$, and Y is the hypercharge. ϕ is the SM Higgs doublet with $\widetilde{\phi} = \epsilon \phi^* = i\tau^2 \phi^*$. The quark weak interactions eigenstates are denoted by

$$q_L = \begin{pmatrix} u_L \\ d_L \end{pmatrix}, \quad u_R, \quad d_R \tag{39}$$

as we did in equation (9) and (10). The effective Wtb vertex including SM contributions and those from dimension-six operators can be parameterised as [8]

$$\begin{aligned} \mathcal{L}_{Wtb} = &-\frac{g}{\sqrt{2}}\bar{b}\gamma^\mu(V_L P_L + V_R P_R)t W_\mu^- \\ &-\frac{g}{\sqrt{2}}\bar{b}\frac{i\sigma^{\mu\nu}q_\nu}{M_W}(g_L P_L + g_R P_R)t W_\mu^- + \text{H.c.} \end{aligned} \tag{40}$$

where q is the outgoing boson momentum, P_R and P_L are the right- and left-handed chiral projection operators, and g_L, g_R, V_R and V_L are couplings. Within SM, only the V_L coupling remains while g_R, g_L and V_R vanish at tree level. The contribution to these couplings from the operators in equation (30) are

$$\begin{aligned} \delta V_L &= C_{\phi q}^{(3)} \frac{v^2}{\Lambda^2}, & \delta g_L &= \sqrt{2}C_{bW}\frac{v^2}{\Lambda^2} \\ \delta V_R &= \frac{1}{2}C_{\phi\phi}\frac{v^2}{\Lambda^2}, & \delta g_R &= \sqrt{2}C_{tW}\frac{v^2}{\Lambda^2} \end{aligned} \tag{41}$$

12

all the new physics on the Wtb can be described by these four parameters. We parameterise the Ztt vertex including the SM contributions in the same vein as with Wtb

$$
\begin{aligned}
\mathcal{L}_{Ztt} = &- \frac{g}{2c_W}\bar{t}\gamma^\mu(X_{tt}^L P_L + X_{tt}^R P_R - 2s_W^2 Q_t)tZ_\mu \\
&- \frac{g}{2c_W}\bar{t}\frac{i\sigma^{\mu\nu}q_\nu}{M_Z}(d_V^Z + id_A^Z\gamma_5)tZ_\mu
\end{aligned}
\tag{42}
$$

with $s_W = \sin\theta_W$, $c_W = \cos\theta_W$ and $Q_t = \frac{2}{3}$ as the top electric charge. X_{tt}^L and X_{tt}^R are couplings in terms of the chiral parts while d_V^Z and d_A^Z are couplings parameterised in terms of vecor and axial parts. In SM only X_{tt}^L contributes, while the three other couplings $X_{tt}^R = d_V^Z = d_A^Z = 0$ at tree level. The contributions from dimension-6 operators are

$$
\begin{aligned}
\delta X_{tt}^L =& \mathrm{Re}[C_{\phi q}^{(3)} - C_{\phi q}^{(1)}]\frac{v^2}{\Lambda^2}, \qquad \delta d_V^Z = \sqrt{2}\mathrm{Re}[c_W C_{tW} - s_W C_{tB\phi}]\frac{v^2}{\Lambda^2} \\
\delta X_{tt}^R =& -\mathrm{Re}[C_{\phi t}]\frac{v^2}{\Lambda^2}, \qquad\quad \delta d_A^Z = \sqrt{2}\mathrm{Im}[c_W C_{tW} - s_W C_{tB\phi}]\frac{v^2}{\Lambda^2}
\end{aligned}
\tag{43}
$$

where $\mathrm{Re}[\dots]$ denotes the real part and $\mathrm{Im}[\dots]$ denotes the imaginary part. The γtt vertex can be parameterised as

$$
\mathcal{L}_{\gamma tt} = -eQ_t\bar{t}\gamma^\mu tA_\mu - e\bar{t}\frac{i\sigma^{\mu\nu}q_\nu}{m_t}(d_V^\gamma + id_A^\gamma\gamma_5)tA_\mu
\tag{44}
$$

where the couplings d_V^γ and d_A^γ are real and related to the top quark magnetic and electric dipole moment, respectively.

$$
\begin{aligned}
\delta d_V^\gamma =& \frac{\sqrt{2}}{e}\mathrm{Re}[c_W C_{tB\phi} + s_W C_{tW}]\frac{vm_t}{\Lambda^2} \\
\delta d_A^\gamma =& \frac{\sqrt{2}}{e}\mathrm{Im}[c_W C_{tB\phi} + s_W C_{tW}]\frac{vm_t}{\Lambda^2}
\end{aligned}
\tag{45}
$$

Thus we have a total of 10 relevant anomalous couplings depending on 7 operator coefficients relevant for electron positron collisions. A more detailed explanation can be found in [8]. Since the physical observables depend on the matrix element squared, we can modify our SM matrix element with our new effective field theory

$$
\mathcal{M}_{SMEFT} = \mathcal{M}_{SM} + \mathcal{M}_{EFT}
\tag{46}
$$

Since the Lagrangian for the sum of dimension-6 are all proportional to changes in the operator coefficients $c_i^{(6)} = c_i$, the dependence can be factored out, giving us the following anomalous matrix element squared

$$
\begin{aligned}
|\mathcal{M}_{SMEFT}|^2 =& |\mathcal{M}_{SM} + c_i^{(6)}\mathcal{M}'_{EFT}|^2 \\
=& |\mathcal{M}_{SM}|^2 + c_i(\mathcal{M}_{SM}^*\mathcal{M}'_{EFT} + \mathcal{M}_{SM}\mathcal{M}'^*_{EFT}) + c_i^2|\mathcal{M}_{EFT}|^2
\end{aligned}
\tag{47}
$$

13

This indicates that the matrix element squared, and thus the cross section, has a parabolic dependence on the operator coefficients $c_i^{(6)}$. When varying a single coefficient we expect to see a parabola, while changing multiple operators will give a more complicated co-linear dependence. However the parabolic behavior can remain while multiple parameters are changed at the same time if they change proportional to each other. Those are exactly the relationships gauge invariance forces between the parameters in equation (41), (43) and (45).
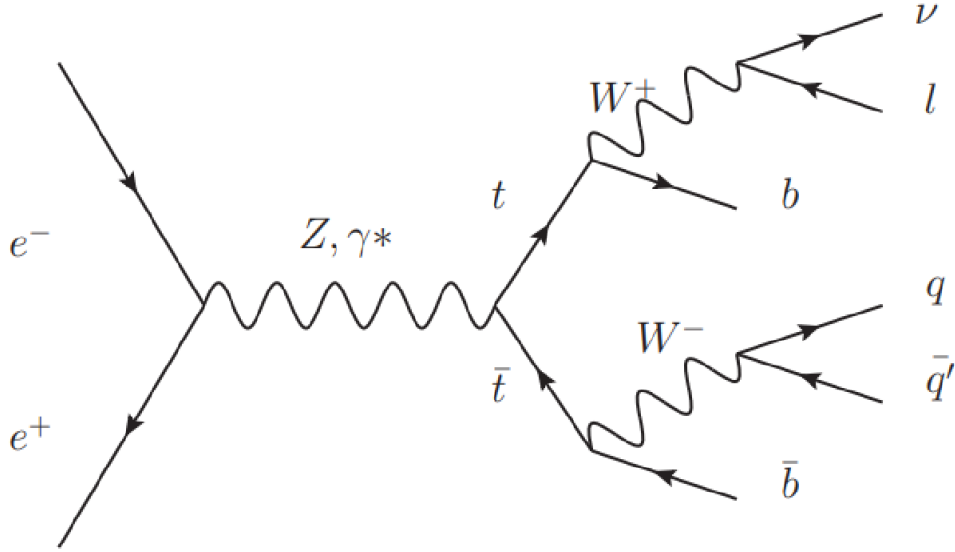
Figure 4: The Feynman diagram for e^+e^- into a semileptonic top event. [4]

Top pair production at e^+e^-

The focus of this study, the top quark, is the heaviest fermion in the SM and the heaviest elementary particle we know of, with a mass of around $m_t \simeq 173\,\mathrm{GeV}$. While the huge mass of the top quark makes it extremely unstable, causing it to decay before it can even form any hadrons, it also makes it an interesting point of study. The Yukawa coupling of the top quark to the Higgs field is given by $\sqrt{2}\frac{m_t}{v} \simeq 0.99$ which is very close to unity. While it might be just a coincidence that the heaviest fermion has a coupling to the Higgs field of 1, it seem like an observation worth investigating and might yield a deeper understanding of the Higgs mechanism and its coupling to fermions. In order to produce top quarks in an experiment the most obvious way is through electron positron annihilation. It is also possible to produce the top quark through other means, but those methods do not produce top quarks in isolation. In the top pair production system, the e^+e^- annihilates into either a virtual photon or a Z boson, which then decays into a $t\bar{t}$ pair. Due to the very large mass of the top quark at around $m_t \simeq 173\,\mathrm{GeV}$, it has an extraordinarily short lifetime, meaning unlike other quarks it decays before hadronization. Additionally, the top quark decays almost exclusively into bW^+ [3]. The W can either decay hadronically $W \to q\bar{q}'$ or leptonically $W \to l\bar{\nu}_l$. This study focuses on semi-leptonic decays, where one W boson decays hadronically and one decays leptonically. The W decays hadronically

67.5% of the time [3], so using simple math we calculate the semi-leptonic case with $2 \cdot 0.675 \cdot (1 - 0.675) = 0.44$, meaning the semi-leptonic case occurs in 44% of cases. These types of decays produce a high energy lepton and neutrino, as well as 4 quarks. The Feynman diagram for the semileptonic decay is shown in figure 4.

The top quark is the only fermion with a mass high enough that it decays into an on-shell W boson, meaning the W boson produced is not a virtual particle and its mass can be found by taking the invariant mass of its decay products. A convenient characteristic of semileptonic the event is that the lepton and the neutrino share an invariant mass of close to the W boson mass at around $m_W = 80.37 \, \text{GeV}$ [2].

It is possible for either the e^+e^- pair to radiate photons or the $t\bar{t}$ pair to radiate photons or gluons. We call these processes initial state radiation and final state radiation, respectively. After the initial decay products have been produced, they hadronize, a QCD process which is not calculable through perturbative QCD, so phenomenological models are used to simulate the process. This hadronization form 4 distinct jets from each of the quarks produced in the semileptonic decay. When the top quark radiates a gluon that decays into quarks, it can form a fifth jet, which can effect the jet algorithms we use later on. After hadronization the unstable particles decay into experimentally observable particles, which is determined by experimentally observed branching ratios. Finally the detector measures the produced particles.

Experimental Apperatus/setup

FCC description

Since the discovery of the Higgs boson in 2012, there has been an increasing interest in a higher precision measurement of both the Higgs boson as well as other elusive particles. This led to the proposal of the Future Circular Collider (FCC), a circular collider with a circumference of 100km, allowing for collisions with centre-of-mass energies up to 100 TeV. The proposed FCC experiment would be divided up into two stages, the FCC-ee experiment, which seeks to study particles like the Higgs boson and the top quark at high precision, and the FCC-hh experiment, which seeks to study the fundamental particles at very high energy collisions. The FCC-ee experiment will focus on e^+e^- collisions and is the focus of this thesis. The two stages of the experiment bears resemblance to the successful LEP-LHC experiment in its design. The Conceptual Design Report (CDR) for the FCC [5] covers the physics discovery opportunities, accelerator design, performance reach, civil engineering, detector designs, technical infrastructure, cost and schedule. The timeline for the construction of the FCC is detailed in Figure 5. The 100 km circumference collider requires a great deal of forethought when choosing where to place it. As such, many aspects are taken into account when considering the placement of the FCC. From the construction of LEP and LHC it has been shown that sedimentary rock, known as molasse, provides very good conditions for drilling, while drilling through limestone pro-
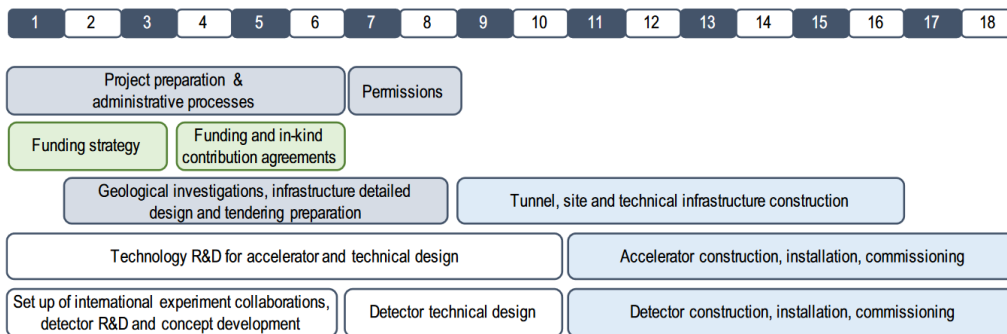
Figure 5: Overview of the FCC-ee implementation timeline starting in 2020. Non technical tasks marked in grey and green are compulsory for any new particle collider project and precede the actual construction. Numbers in the top row indicate the year. Physics operation would start in 2039 according to this schedule [5].

17

vides significant problems. As such the placement of the FCC seeks to minimize the amount of limestone and maximize the amount of molasse in its path. Another concern was minimizing the depth of the collider shaft in order to reduce pressure on the underground structures. The depth of lake Geneva was also a concern. These concerns led to the definition of the study boundary, shown in figure 6, wherein the FCC must be placed. Figure 6 also shows the proposed placement of the FCC.

When the LHC observed the production of the Higgs boson in 2012 for the first time, it was at a mass well compatible with this prediction in the context of the SM. Similarly, the measured W mass m_W and the weak mixing angle θ_W are also very compatible with the SM. The current overall situation of the SM fit to the precision measurements available to date is summarised in Figure 7a. The issue with this global fit is that there are many experimental facts that are not explainable with the SM, such as as dark matter, the cosmological baryon-antibaryon asymmetry and the neutrino masses. The FCC-ee seeks to test the global fit at an unprecedented level of precision. A theoretical global fit with the expected FCC-ee experimental data is shown in figure 7b, where the global fit would be unable to support the current SM, providing exciting opportunities for new physics.
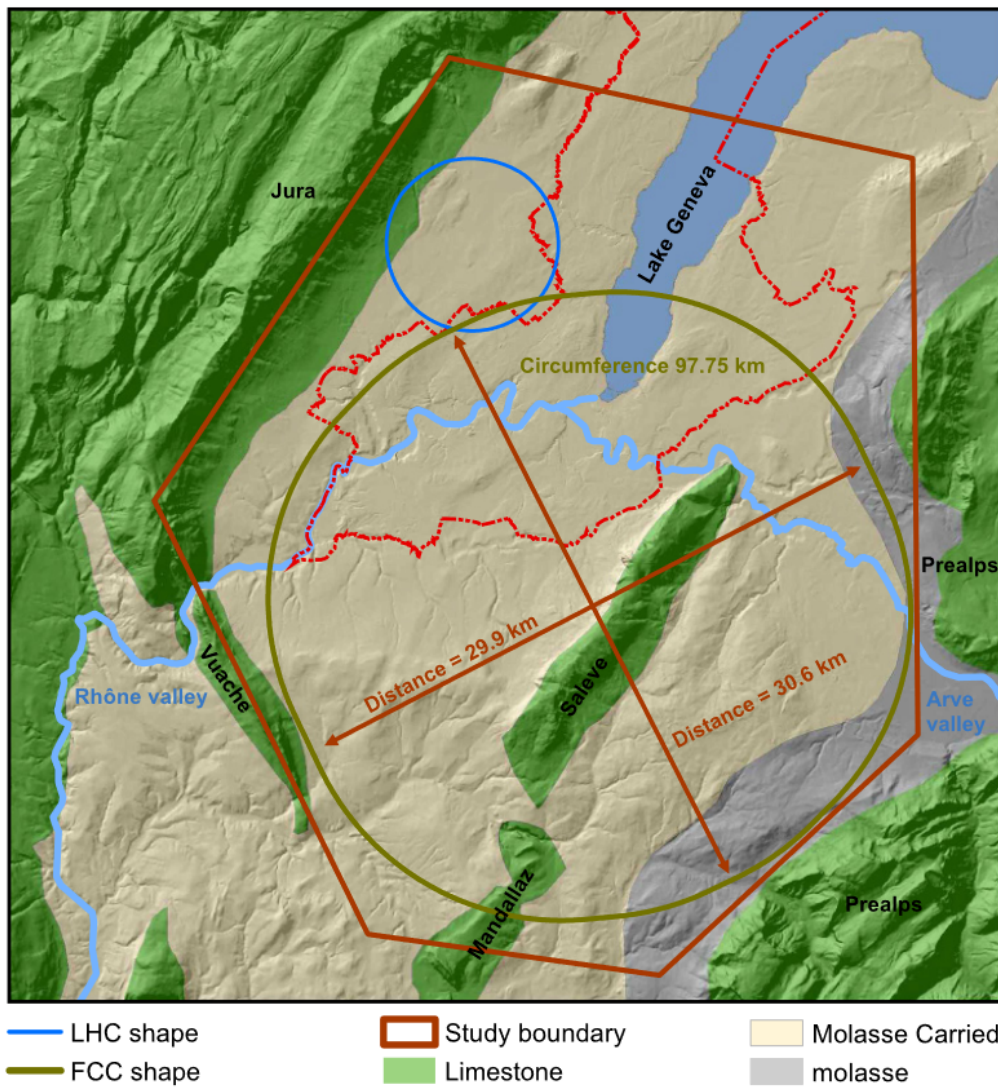
Figure 6: The proposed location and size of the FCC with geological and topographical information [5]. In this case, the circumference of collider is 97.75km [5].
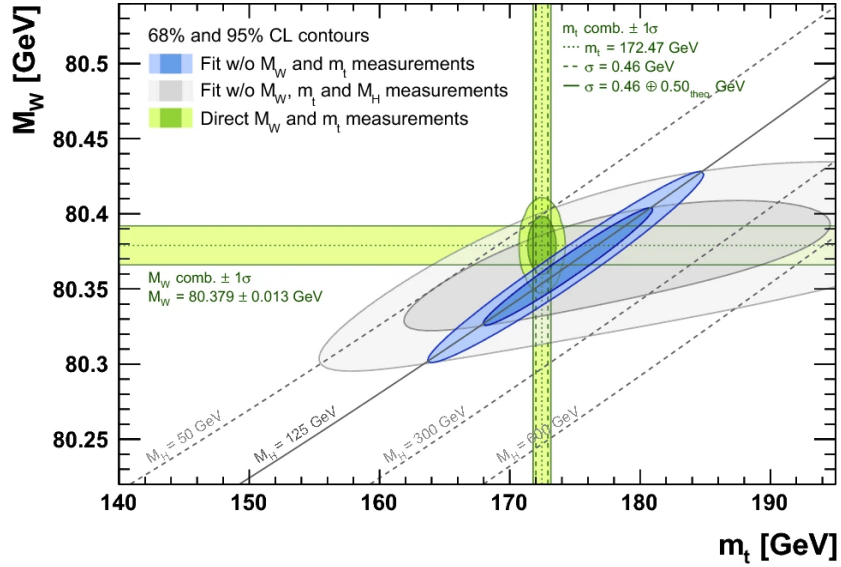
(a) Contours of 68% and 95% confidence level obtained from fits of the standard model to the precision measurements available to date, in the (m_t, m_W) plane. The grey area is the result of the fit without the direct measurements of the W, top, and Higgs masses, while the narrower blue area includes the Higgs boson mass measurement at the LHC. The horizontal and vertical green bands and the combined green area indicate the 1σ regions of the m_W and m_t measurements [24].
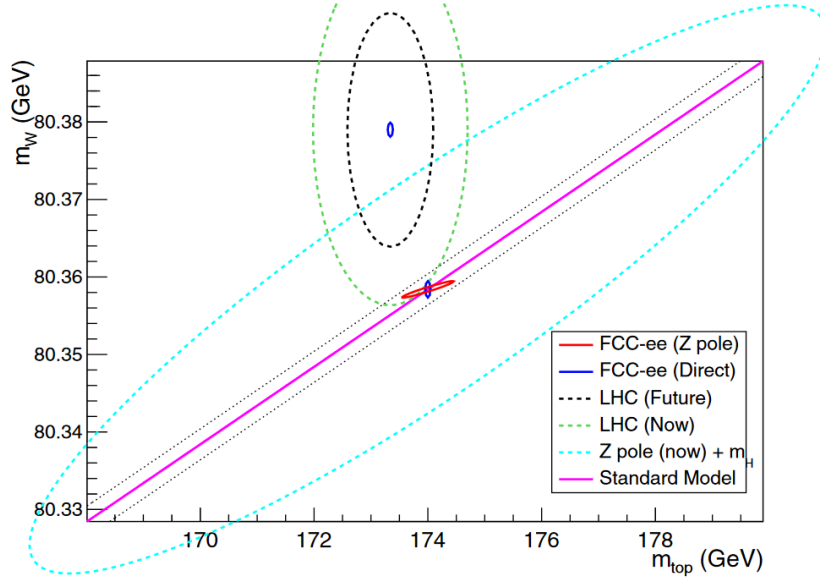
(b) Contours of 68% confidence level as in figure 7a from fits of the SM expected from expected measurement in the FCC-ee. [5]

Figure 7

20

Parameter	Z	WW	ZH	$t\bar{t}1$	$t\bar{t}2$
Beam energy (GeV)	45.6	80	120	175	182.5
Bunches / beam	16640	2000	328	59	48
Average bunch spacing (ns)	19.6	163	994	2763	3396
Bunch population (10^{11})	1.7	1.5	1.8	2.2	2.3
Energy loss / turn (GeV)	0.036	0.34	1.72	7.8	9.2
Run time (year)	4	2	3	1	4
Integrated luminosity (ab^{-1})	100	10	5	0.2	1.5

Table 1: Machine parameters of the FCC-ee for different beam energies.

Expected running conditions at the FCC-ee

The FCC-ee's focus on precision is important for determining the validity of the standard model. This gives the FCC-ee a focus on improving the luminosity of the experiment. Luminosity, the amount of collisions over a set timeframe, gives a higher precision, since the more collisions are performed the more precise the measurement of the experiment will be. An overview of the expected performance of the FCC-ee for different beam energies is shown in table 1.

Since we dont know where we might find new physics, the FCC-ee aims to have as broad a scope as possible, examining many different physics processes. The main centre-of-mass operating points for the FCC-ee are around 91 GeV (Z-pole), 160 GeV (W-pair production threshold), 240 GeV (Higgs factory) and 340-365 GeV (at and above the $t\bar{t}$ threshold). At the $t\bar{t}$ threshold a scan over the energies between $340\,\text{GeV}$ and $350\,\text{GeV}$ around $2m_t$ would be performed.

This study will focus on the $e^+e^- \rightarrow t\bar{t}$ process at a centre-of-mass collision energy of $\sqrt{s} = 365\,\text{GeV}$, which will run for a total of 4 years. The FCC-ee aims for a luminosity of at least $\mathcal{L} = 1.5\text{ab}^{-1}$ for a centre-of-mass collision energy of $\sqrt{s} = 365\,\text{GeV}$.
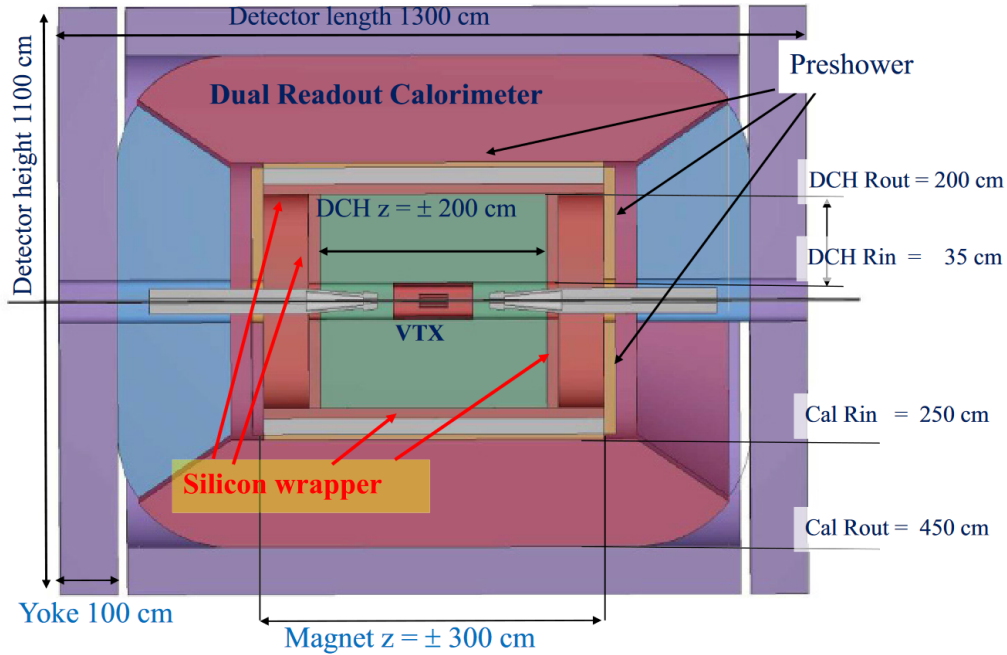
Figure 8: The IDEA detector

The IDEA detector

The Innovative Detector for Electron-positron Accelerator (IDEA) is one of the proposed detector concepts which has been developed for FCC-ee. The predicted detector performance is demonstrated in the FCC-CDR [5], yet there are still aspects of the design that needs to be finalized.

The innermost detector, surrounding the beam pipe, is a silicon pixel detector. These very light detectors with high resolution are the basis for the vertex detector, which will be used in b- and c-tagging. The drift chamber surrounds the vertex detector. It is large-volume extremely-light short-drift wire chamber which extends from a inner radius of $R_{in} = 0.35$m to an outer radius of $R_{out} = 2$m for a length of $L = 4$m and consists of a total of 56448 drift cells. The chamber is operated with a very light gas mixture, 90% He - iC_4H_10 (isobutane), which is designed to improve tracking by allowing cluster counting and timing techniques to be employed to improve both spatial resolution and particle identification. The angular coverage of this chamber extends down to 13°. A layer of silicon micro-strip detectors surround the outside of the drift chamber providing an additional accurate space point as well as precisely defining the tracker acceptance. The IDEA tracking system is expected have a spatial resolution better than 100μm, a transverse mo-

mentum resolution of $\sigma(1/p_T) \simeq a \bigoplus b/p_T$, with $a \simeq 3 \times 10^{-5}\,\text{GeV}^{-1}$ and $b \simeq 0.6 \times 10^{-3}\,\text{GeV}$ and angular resolutions of better than 0.1 mrad in both azimuthal and polar angle for momenta exceeding $10\,\text{GeV}$.

The 2T magnetic field is provided by a thin, low-mass superconducting solenoid coil that sits just outside the tracking chambers in the barrel region. It works as an absorber of about $1X_0$, is followed by one layer of Micro Pattern Gas Detector (MPGD) chambers, another $1X_0$ absorber and a second layer of MPGD chambers. The MPGD chamber layers acts as a preshower detector which provides tracks to be matched to calorimeters showers in case they are close. After the preshower layers is the lead-fibre dual-readout calorimeter. The calorimeter is $2\,\text{m}$ deep and the total number of fibres is in the order of 10^8. the calorimeter is sensitive to scintillation light and Cherenkov light which provides good energy resolution for both electromagnetic and hadron showers, providing a resolution close to $10\%/\sqrt{E}$ for isolated electrons and $30\%/\sqrt{E}$ for isolated pions. The outermost layer is the muon chambers which sits within a magnet return yoke. The yoke protects the beams and limits the impact on the luminosity from the magnetic field. There is still additional work that needs to be done to finalize the design of the IDEA detector. For example, the magnet system requires a significant R&D effort in order to make the solenoid be made much smaller, ultra-thin and radiation-transparent [5]. The clean experimental environment of an electron-positron collider allows the detector to run on a so called "triggerless" scheme, since the initial state is known with every event any processed data can be accepted as an event. This scheme could be similar to previous electron-positron colliders, but the feasibility of such a scheme is under investigation.

Simulation framework

This study is performed using a simulated data that has been generated using the Future Circular Collider Software (FCCSW). FCCSW uses several modular components, of which the components important for this study are `Delphes`, `Pythia8` and `EDM4HEP` which all fall under the `Key4HEP` framework [14]. `Key4HEP` aims to be the complete software solution for the full experiment life-cycle of several future colliders, such as the FCC, the Circular Electron Positron Collider (CEPC), the Compact Linear Collider (CLIC) and International Linear Collider (ILC). `Key4HEP` seeks to gather software components and tools into one common framework that can be tailored to each specific experiment. `Key4HEP` also makes sure the different experiments use a common Event Data Model in the form of `EDM4HEP`, creating ease of access of data. `EDM4HEP` is a data model that specifies how data in the output files is structured. The Monte Carlo samples are generated by calling the `DelphesPythia8_EDM4HEP` command with a `Delphes` card relating to the IDEA detector and a `Pythia` command card that specifies the event characteristics. With `Pythia` the hard processes are specified, the amount of events simulated at a collision energy are selected and effects like initial state radiation is specified. `Pythia` then generates the Monte Carlo samples and simulates the decays and hadronization. `Delphes` then reconstructs the particles using fast detector simulation using the environment described in the IDEA detector card. From the `Delphes` process an `EDM4HEP` output file is created. The data is stored and handled using `ROOT`. `ROOT` is a framework for data processing developed by CERN. `ROOT` can save, access and analyze very large amounts of data at fast speeds.

The `ReconstructedParticles` framework

`Pythia8` is used to generate simulated event samples and compute cross sections for hard scattering an decay processes of particles at high-energy colliders. `Pythia` can simulate particle collisions to a large variety of specifications. `Pythia` can select the hard process of a collision event and calculate its effective cross section, specify additional parameters such as initial state radiation (ISR) and final state radiation (FSR), change the masses of particles and specify which types of decays are permitted, including some not in the SM. `Pythia` generates Monte Carlo data and hold information about all of the event particles at all stages before detection. A weakness of `Pythia` is in its inability to select hard processes of higher order perturbation theory, which is one of the reasons we must also use `Whizard` in our simulations. An overview of `Pythia` can be found here [22].

Whizard is another program that can simulate particle physics [16]. The advantages of Whizard is its ability to simulate higher order SM processes as well as the anomalous coupling terms. The 10 coupling parameters relating to the dimension-six operators relevant to our top interactions exists within Whizard via Feynman rules in a predefined model named "SM_top_anom". The parameters from (41), (43) and (45) has its corresponding Whizard parameter specified in table 2. The parameters are linked to other parameters by way of the internal operators from equation (30) and which Whizard calculates internally. Due to the 10 parameters being dependent on 7 operators we only have 7 degrees of freedom, meaning we can only variate 7 parameters, while three of the parameters are fixed in order to retain gauge invariance. The choice of which parameters to keep fixed is based on the work in [9] and [10]. Delphes is a C++ framework performing a fast multipurpose

Parameter	Coupling	Gauge freedom
vr_tbW_Re	δV_L	Free
vl_tbW_Re	δV_R	Free
tl_tbW_Re	δg_L	Free
tr_tbW_Re	δg_R	Free
tv_ttA	δd_V^γ	Free
ta_ttA	δd_A^γ	Free
vr_ttZ	δX_{tt}^R	Free
vl_ttZ	δX_{tt}^L	Fixed
ta_ttZ	δd_A^Z	Fixed
tv_ttZ	δd_V^Z	Fixed

Table 2: List of model parameters and their corresponding expressions in equations (41), (43) and (45). "Free" means the variable can be freely changed, while "Fixed" means it is internally calculated depending on the other parameter values.

detector response simulation for collider experiments. This simulation includes a tracking system, calorimeters and a muon system. The simulation of the detector response takes into account the effect of magnetic field, the granularity of the calorimeters and sub-detector resolutions [15]. Delphes

performs a fast simulation of detectors, which unlike a total simulations only approximately simulates the detector. This is necessary in our case, since many of the details of the IDEA detector is yet to be finalized. `Delphes` is modular in its design and can couple to both `Pythia` and `Whizard` as well as output its data into the `EDM4HEP` format we are interested in. `Delphes` takes our input, simulates the IDEA response, reconstructucts our particles and saves our simulated particles as `ReconstructedParticles`. These are the detected particles. When referring to the "true" simulated particles, we call them Monte Carlo (MC) particles. Not every MC particle is detected by the detector and many of the particles are detected with 4-momentum differing from the MC particle momentum and sometime the detector detects non-existant particles. When handling the MC particles and reconstructed particles, we use `FCCAnalyses`.

`FCCAnalyses` is a common framework for FCC related analyses, using `EDM4HEP` input `ROOT` files for analysis and production of plots [12]. As part of this thesis, minor functionalities were developed for `FCCAnalyses` that help identify the MC particles associated with the reconstructed particles. `FCCAnalyses` has a Jet Clustering Interface which uses `FastJet`, a software package for jet finding in high energy collisions. `FastJet` was mainly developed for hadron collider experiments, but it also supports algortihms for lepton collider experiments. `FastJet` provides a variety of jet algorithms for e^+e^- collisions. Previous analysis of jet algorithm for the semileptonic top decay at FCC-ee shows a favourable outcome in choosing the Durham algorithm with 4 exclusively clustered jets, so that is the algorithm we choose [10]. Details on the Durham algorithm, also called k_t algorithm for e^+e^- collisions, can be found in the `FastJet` user manual [17].

Event selection & reconstruction

After simulating our $t\bar{t}$ events, we want to reconstruct the events and identify the 4-momentum of the top particle, the bottom particle and the W boson. This is possible thanks to the fact that in a e^+e^- collision, we know the initial state of the system. One issue arises when you consider that while it is possible in the simulation framework to simulate any collision event desired, in experiments we don't get to select the processes that take place in the detector. In order to correctly perform our analysis on simulated events we need to take background events into account by simulating them and adding them to our $t\bar{t}$ sample before we perform our analysis. Since the cross section of top pair production is lower than many other processes, the amount of background events will far overshadow the signal events, meaning we will need to perform an event selection to differentiate between them.

The plan is to use machine learning algorithms to classify events as either background or signal. Before that method is used we will perform a manual *pre-selection*, where we ensure that we have the necessary tools for reconstruction later on. This also gets rid of the most obvious background events. Once the event selection has been completed, machine learning is used to identify any possible initial state radiation particles and remove them from the event, after which the event is reconstructed through a *Kinematic Fit*.

Over the four year run of the FCC-ee at $\sqrt{s} = 365$ we expect an integrated luminosity of 1.5ab^{-1}. In order to approximate the expected amount of events for a given type of particle collision, we simply use the following formula

$$N_{expected} = \mathcal{L} \cdot \sigma \tag{48}$$

where $\mathcal{L}$ is the integrated luminosity and σ is total cross section of the event at the relevant centre of mass energy. Using `Pythia` we can get the cross sections of these events. Table 3 shows a summary of the $t\bar{t}$ process, relevant processes that can occur, their cross sections and number of expected events given the integrated luminosity $\mathcal{L} = 1.5\text{ab}^{-1}$. These processes have been simulated using `Pythia`, with the execption of the ZWW, the ZZZ and the single top events, which had to be simulated using `Whizard`. One relevant process that is not included is the $e^+e^- \rightarrow \gamma Z$. This is due to the process being poorly defined within `Pythia` when including initial state radiation. The contribution to the background sample is not small but can be reduced through event selection. In order to perform analysis of the ISR contribution we are forced to neglect the contribution of γZ events in this study.

Process	$\sigma[\text{pb}]$	$N_{expected}$
$t\bar{t}$	0.452 ± 0.003	678000
$b\bar{b}$	4.065 ± 0.0008	6097500
$q\bar{q}$	17.03 ± 0.002	25545000
$\mu^+\mu^-$	1.902 ± 0.0005	2853000
$\tau^+\tau^-$	1.901 ± 0.0005	2851500
W^+W^-	11.20 ± 0.001	16800000
ZZ	0.8565 ± 0.0003	1284750
ZH	0.1296 ± 0.0001	194400
ZZZ	$(7.644 \pm 0.026) \cdot 10^{-4}$	1146
ZWW	$(1.594 \pm 0.002) \cdot 10^{-2}$	23850
Single top	$(4.572 \pm 0.012) \cdot 10^{-3}$	6850

Table 3: Relevant processes and their statistics at $\sqrt{s} = 365$ and $\mathcal{L} = 1.5\text{ab}^{-1}$.

$t\bar{t}$ event characteristics

In order to distinguish between signal and background we analyze the observables and their features in $t\bar{t}$ events. We are not just interested in the top quark event, but the semi-leptonic decay mode of the top quark, since those events are useful when attempting a reconstruction of the event. The semileptonic decay mode is the decay where one of the two W decay bosons decays into leptons and the other decays into hadrons. This decay mode is written as

$$e^+e^- \rightarrow t\bar{t} \rightarrow b\bar{b}q\bar{q}'l\nu_l \tag{49}$$

The semileptonic top quark event has a branching ratio of 44%, meaning if $N_{top} = 678000$ then $N_{semileptonic} \approx 298000$. The semileptonic decay of the $t\bar{t}$ pair produces 6 identifiable objects, the lepton, the neutrino, 2 b-quarks and 2 light flavour quarks (d, u, s, c). The nearly undetectable neutrino can be identified by assigning the total 4-momentum lost in the collision, the missing momentum, to the neutrino. The quarks will hadronize in an experiment and produce clusters of hadrons in particle jets, giving us a total of 4 jets. The two jets produced by light flavour quarks will essentially be indistinguishable from each other, while the b-jets will be distinguishable from the other jets by its associated W boson. Since the W bosons are produced on-shell, the invariant mass of the two light flavour jets and the invariant mass of the lepton and neutrino should both approximately be equal to the W boson mass at $m_W = 80.37$ [2]. This is one of the advantages of the semileptonic

decay mode: the two W boson can easily be distinguished from one another, since in hadronic cases the light quark jets will not be easily distinguished from one another and in fully leptonic cases the undetected neutrinos cannot easily be reconstructed from the missing momentum.

In semileptonic events there can be multiple observed leptons. The lepton from the $W \to l\nu_l$ decay process is assumed to carry the highest energy of all the leptons, since that lepton was generated at an earlier stage of the decay chain. By creating a "Highest Energy Selector", the highest energy lepton of a top event can be selected. Figure 9 shows the energy of the highest energy lepton (if there are any) from a sample of 1 million simulated $t\bar{t}$ events at $\sqrt{s} = 365\,\text{GeV}$. The graph distinguishes between hadronic decay cases (red) and in semileptonic and fully leptonic cases (blue). Even though hadronic cases are the majority of events at a branching ratio of 45.5%, there a very few leptons produced in those cases, and those leptons are of low energy compared to the leptonic cases.

Lepton universality is assumed, meaning it is equally likely for a the W to decay to any of the three leptons $l = \{e, \mu, \tau\}$. In collider experiments electrons and muons can usually be quite easily identified in the detector. The tau particles are special due to their high mass, and since the lifetime of a particle is inversely proportional to its mass to the fifth power $\tau_\tau \propto (m_\tau)^{-5}$ the tau particles will decay before exiting the detector. The tau decays through the W boson and its decay modes are $\tau^- \to e^- \bar{\nu}_e \nu_\tau$ (17.4 %), $\tau^- \to \mu^- \bar{\nu}_\mu \nu_\tau$ (17.4 %), $\tau^- \to \pi^- (n\pi^0)\nu_\tau$ (48 %) and $\tau^- \to \pi^- \pi^+ \pi^- (n\pi^0)\nu_\tau$ (15 %) where n is usually between 0 and 2 [3]. Only 34.8 % of the time will we be able to identify a lepton from the tau decay, meaning we expect that at least 21.7 % of semileptonic event will not even have a high energy lepton, if any lepton at all.

When identifying the neutrino, we add the total 4-momentum of the system and subtracts it from the initial state 4-momentum vector $\vec{p}_i = (0, 0, 0, 365\,\text{GeV})$. The momentum vector we end up with is the expected momentum vector of the neutrino. The IDEA detector has a small hole where the electron positron beams enter that inevitably some of the produced particles will fly out of. Any particles with an angle of $\theta = 0.1$ to the electron beam will fly out of the detector hole and be undetected. This will effectively reduce the accuracy our identification of the neutrino.

Event selection

To differentiate between the signal events and the background events, machine learning is used. In order to improve the distinguishing of events a pre-selection is performed which intends to sort the most obvious of back-
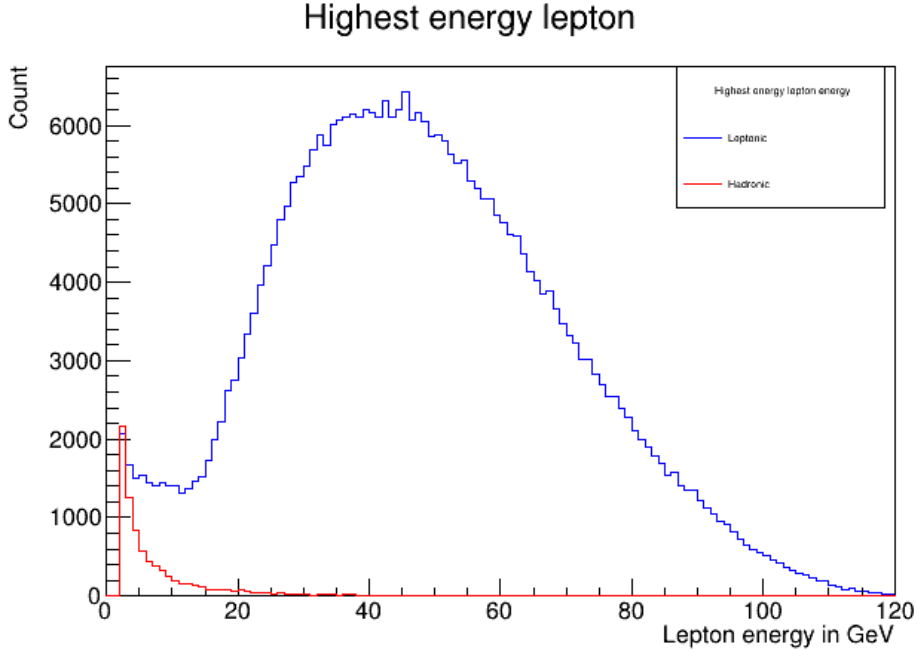
Figure 9: The highest energy lepton detected for 1 million simulated $t\bar{t}$ events. We distinguish between events where at least one of the W bosons produced in the top decay decayed leptonically (blue) and those where neither of them did (red).

grounds events from the rest. Additionally, when reconstructing the event we have to require being able to identify a lepton and four jets.

Since we are in the semileptonic case, we only consider those types of events as our signal events. Every other type event is considered as a background event. When discussing the event selection and how many events were selected of each type, it is useful to define the efficiency ε and the purity P

$$\varepsilon_S = \frac{S}{S_{total}}, \quad P = \frac{S}{S + B} \tag{50}$$

where S is the signal accepted, B is the background accepted and S_{total} is the total signal. Before any event selection has been made the efficiency trivially is $\varepsilon_S = 1.0$ while the purity for our event is $P = 0.0053$.

Since we plan to use machine learning for most of the event selection, we need a pre-selection to both make sure we have the lepton and the four jets needed for reconstruction of the event, as well as to improve the performance of the machine learning algorithm.

Since the lepton from the $W \to l\nu_l$ decay is assumed to have a high energy, we require that the event has at least one high energy lepton. Requiring a lepton will also be necessary for the later analysis where a kinematic fit will be performed. In order to define the energy required for a lepton to be a "high energy" lepton, figure 9 is used. As can be seen, there appears to be a large difference between in the amount of events under and over 20 GeV, as well as hadronic event mostly having leptons of under that energy. From this observation a cutoff for high energy lepton of 10 GeV is chosen, such that only events that have a lepton of at least 10 GeV are accepted. The highest energy lepton of these events are isolated, such that it is not used to construct jets with. If there are additional lepton over 10 GeV, that are also accounted for for later analysis.

Requiring an identified lepton gets rid of a lot of signal events, since we expect it to get rid of at least 21.7 % of semileptonic events from the hadronic tau decays. Requiring a lepton gives us an efficiency of $\varepsilon_S = 0.59$, meaning requiring just a single identified lepton costs us 0.41 % of signal events, which is much larger than the expected 21.7 %. The reason is that when the detector simulation attempt to identify leptons it does not always succeed. Around ~ 18 % of the semileptonic decay events are not identified by `Delphes` as a lepton. Without an identified lepton we cannot reconstruct the event and must reject the event. The remaining ~ 1 % lost is most likely due to leptons that flew out of the detector hole or otherwise evaded detection. After also requiring that at least one identified lepton has an energy of at least 10 GeV the efficiency becomes $\varepsilon_S = 0.565$.

After events with at least one high-energy lepton has been selected, use the Durham jet algorithm from `FastJet` with exclusive clustering such that exactly 4 jets are created. In the case where it is not possible to create 4 jets (such as when the event has less than 4 reconstructed particles), the event is discarded, since the 4 jets will be necessary for reconstruction of the event later on. This requirement doesn't get rid of any signal events.

To finalize the preselection and further distinguish between signal and background, we place a cut on the amount of charged tracks, the trajectory of electromagnetically charged particles reconstructed by `Delphes`. We require that a minimum of 10 charged tracks to be reconstructed, a conservative number, considering that we expect dozens of charged particles. This is a gets rid of some of the most obvious background events. Table 4 gives an overview of the effect of the preselection cuts had on the signal and different types of background events. The most numerous types of background events at this point are the W^+W^- and ZZ events.

After the total preselection the signal efficiency $\varepsilon_S = 0.565$ and the purity is $P = 0.188$, which is already a significant improvement from the original

sample. Now that the preselection has been completed, it is time to perform an event selection using machine learning algorithms from `ROOT`.

Process	Before preselection (10^3)	After preselection (10^3)
Semileptonic $t\bar{t}$ decay	297.4	168.1
Other $t\bar{t}$ decays	380.6	60.6
$b\bar{b}$	6097.5	25.19
$q\bar{q}$	25545	12.1
$\mu^+\mu^-$	2853	0.13
$\tau^+\tau^-$	2851.5	0.07
W^+W^-	16800	411.6
ZZ	1284.8	174.7
ZH	194.4	30.4
ZZZ	1.14	0.23
ZWW	23.85	9.34
Single top	6.850	3.35

Table 4: Total amount of events before and after the preselection for both signal and background events.

Machine learning with TMVA

In order to perform the last of the event selection, machine learning is used to get rid of the most ambiguous of background events. The Toolkit for Multi-Variable Analysis (TMVA) is the `ROOT` library that provides the interfaces and implementations of different multivariate classification machine learning techniques [20]. We will be using this library for classifying events as either signal events or background events. The machine learning algorithms in TMVA need to be trained on signal and background before they can classify events as one or the other. Before we can get stated we need to consider which parameters the algorithms will use to analyze the events and which algorithm should be used for the event selection. As mentioned previously, a preselection was performed. This is partly because if the machine learning algorithm is trained on background events trivially classified as such, it will place an equal weight on distinguishing the obvious events and the ambiguous events when it should be placing more weight on the ambiguous events. Before we can get started with TMVA, we need to determine which parameters we want to train on. These parameters should have physical reasons for

being able to distinguish between signal and background. We have already given reason why the energy of the highest energy lepton and the amount of charged tracks are important for distinguishing events, so we will also be using those parameters for training. In order to sort fully leptonic events as well as some background events like tau or muon production, the energy of the second highest energy lepton with $E_{l,2nd} > 10\,\text{GeV}$ is selected as a parameter. The thrust of the event is also a selected parameter. The thrust of an event is a measure used to quantify the event shape and is defined as [23]

$$T = \max \frac{\sum_i |\vec{p}_i \cdot \hat{n}_T|}{\sum_i |\vec{p}_i|} \tag{51}$$

where $|\vec{p}_i|$ are the particle momenta and $\hat{n}_T$ defines the thrust axis that maximises the energy flow [19]. We expect the lepton-neutrino pair and the two jets produced by light quarks to have invariant masses ($m_{l,\nu}$ and m_{jets}, respectively) near the mass of the W boson. Additionally when the jet algorithm makes 2 jets out of what should have been 1 jet, the invariant mass of those two jets are usually low. The general expectation is therefore that there will be a lot of information to be extracted from those variables. The missing energy of the event is also a variable to consider. Energy conservation tells us that the total energy of the decay particles should be equal to the initial energy $\sqrt{s} = 365\,\text{GeV}$. Events with high energy neutrinos are expected to have an energy much lower than the initial energy, since the undetected neutrinos carried that energy. The semileptonic event has exactly one high energy neutrino to take into account, meaning the missing energy is also a good parameter. We also look at the invariant mass of every reconstructed particle except the lepton, m_{rest}, which we also expect to be comparably high due to the production of massive particles. An overview of the parameters used is shown in table 5 and has taken much inspiration from [10], which performed manual cuts on the same parameters.

After determining the variables that will be used, the machine learning algorithm has to be determined. TMVA offers many different classification algorithms, but for this section we examined 4 methods: Boosted Decision Tree (BDT), Projective likelihood estimator (Likelihood), K-Nearest Neighbors (KNN) and Rectangular cut optimization (Cuts). An examination on the efficiency of the algorithms it becomes clear that BDT is superior in this case. Figure 11 shows the rejected background as a function of the signal (also known as a ROC curve), wherein it can be seen that BDT is more efficient at distinguishing the background from the signal in all cases except fringe cases where the efficiency is near 0 or 1. For our classification we will be using BDT.

Correlation Matrix (signal)

	E_l	$E_{l,2nd}$	T	m_{rest}	E_{miss}	$m_{l,\nu}$	m_{jets}	N_{tracks}
N_{tracks}	-1 / -15	-2 / 8	-8 / -20	22 / 34	-17 / -10	-22 / -13	13 / 50	100 / 100
m_{jets}	-8 / -15	-1 / 16	-33 / -26	40 / 51	-24 / -19	-24 / -15	100 / 100	13 / 50
$m_{l,\nu}$	2 / -18	3 / -12	/ -19	-60 / -34	58 / 69	100 / 100	-24 / -15	-22 / -13
E_{miss}	-64 / -68	2 / -30	-1 / -9	-59 / -43	100 / 100	58 / 69	-24 / -19	-17 / -10
m_{rest}	-19 / -26	-3 / 42	3 / -17	100 / 100	-59 / -43	-60 / -34	40 / 51	22 / 34
T	-1 / 8	/ -23	100 / 100	3 / -17	-1 / -9	/ -19	-33 / -26	-8 / -20
$E_{l,2nd}$	1 / 10	100 / 100	/ -23	-3 / 42	2 / -30	3 / -12	-1 / 16	-2 / 8
E_l	100 / 100	1 / 10	-1 / 8	-19 / -26	-64 / -68	2 / -18	-8 / -15	-1 / -15

Figure 10: The Correlation matrix from the variables in table 5. The black numbers tell the correlation between signal parameters while the red numbers tell the correlation between the background parameters. The colors are based on the signal correlation matrix. Negative numbers means the parameters are anticorrelated. This demonstrates both how much information is added with each parameter as well as how the correlation might differ from signal to background. While there is a slight correlation between N_{tracks} and m_{jets} for signal events, the correlation is much larger for background event, giving additional information that is nontrivial for manual cuts.

Parameter	Description
E_l	Energy of the highest energy lepton
$E_{l,2\text{nd}}$	Energy of the 2nd highest energy lepton with $E > 10 GeV$
T	Thrust of the event
m_{rest}	Invariant mass of reconstructed particles (excluding the HE lepton)
E_{miss}	Missing energy of the event
$m_{l,\nu}$	Invariant mass of the HE lepton and misssing 4-momentum (neutrino)
m_{jets}	Smallest invariant mass between two jets
N_{tracks}	Amount of charged tracks able to be reconstructed

Table 5: Parameters used to distinguish between events in the TMVA machine learning algorithms.

The BDT machine learning algorithm works by creating *decision trees*, which are binary trees where repeated yes/no decisions are taken on a single parameter a time until some condition is met, such as classifying an event as signal or background. Figure 12 shows a decision tree. *Boosting* a decision tree extends this concept to several trees that are derived from the same training sample by re-weighting events then are combining them into a single classifier which is given by a single weighted average of all the trees. The specifics of how the algorithm works can be found in the TMVA user manual [20].

The BDT algorithm is trained on a sample of already classified signal and background events with an amount of events equal to half of number of pre-selected events. When the training has completed a file that stores the weights of the final decision tree is created, which can be used to classify events to a specified efficiency. In order to classify events we need to choose a desired efficiency of our event selection. A good baseline for this is to optimize for the signal efficiency times the purity $\varepsilon_S \cdot P$. Optimizing for this value we get a signal efficiency of $\varepsilon_S = 0.965$ and a purity of $P = 0.923$ for the algorithm, which are very good numbers compared to a manual cut selection. This brings the total signal efficiency of the preselection and TMVA to $\varepsilon_S = 0.548$.
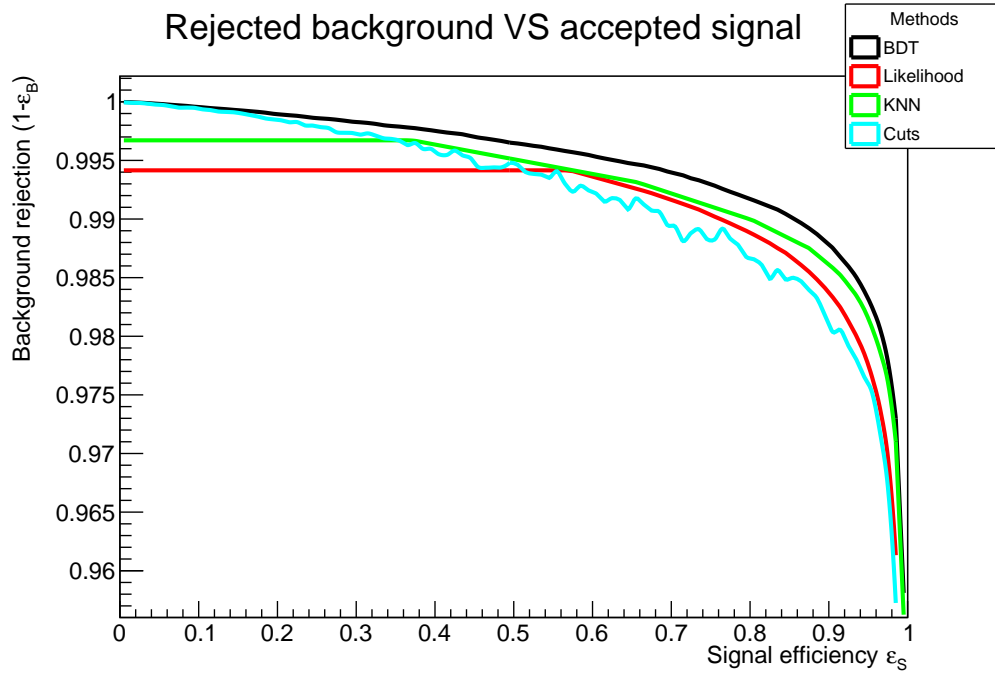
Figure 11: The rejected background as a function of signal efficiency for the four tested machine learning algorithms. BDT essentially always has the highest background rejection for a given signal efficiency.
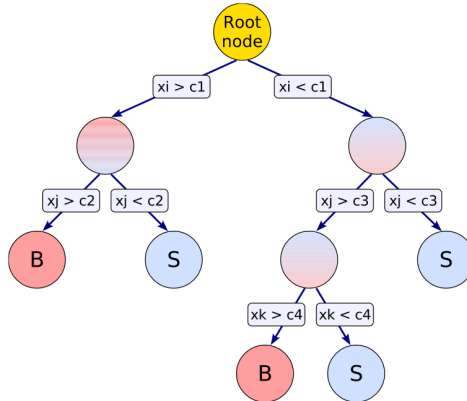
Figure 12: Schematic view of a decision tree, the type of selection algorithm that the BDT method is based on. Starting from the top, at each node the data is split into one of two categories by comparing its values x to a parameter c_i until it is either labeled as signal (S) or background (B) [20].
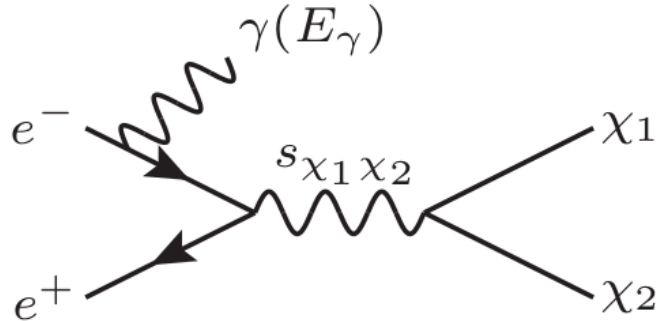
Figure 13: Feynman diagram showing initial state radiation in a e^+e^- collision.

Isolating initial state radiation.

Initial state radiation (ISR) is when the e^+e^- pair emit a photon before annihilation, thus changing the initial state conditions of the collision. This means that a total reconstruction of the event will be inaccurate and we will have difficulty when making a kinematic fit of the event. For this reason we have an interest in isolating and removing these ISR photons from the event. The method we use to identify these photons is by using TMVA to train machine learning algorithms on photons to classify them as either ISR or decay photon. A sample of 50000 semileptonic events was generated to train the algorithms on photons. Taking all of the ISR and decay photons from semileptonic events as our signal and background, the purity is $P = 0.0055$. Similarly to the event selection we are going to perform a pre-selection on our photons to make sure that the relevant photons are selected. First, the photons need to be identified, which is done by taking all reconstructed particles which are both chargeless and massless. Since low energy photons will have a negligible effect on the reconstruction of the event, we are mostly interested in photons of high energy. We also expect there to be a lot of low energy photons in the event, so in order to help the training algorithm in distinguishing between the ISR we are interested and the decay photons we are not interested in, we choose to only train on photons with energy higher than $2.0\,\text{GeV}$. This cut gives a signal efficiency of $\varepsilon_S = 0.758$ and a purity of $P = 0.0063$.

Many of the photons generated in the event are going to be generated from the π^0 meson. The π^0 meson predominantly decays into two photons

37
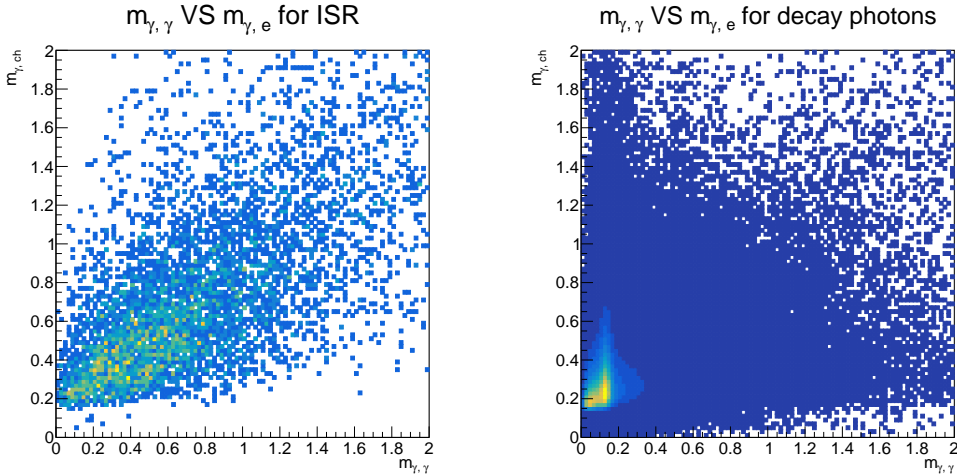
Figure 14: The smallest invariant mass between two photons $m_{\gamma,\gamma}$ plotted against the smallest invariant mass of the photon to a charged particle $m_{\gamma,ch}$ for ISR photons (left) and decay photons (right). The photons are drawn from the same sample of ~ 50000 semileptonic events. The ISR photons number 6737 while the decay photons number 1235510.

$\pi^0 \to \gamma\gamma$. These photons are expected to be relatively close to each other, while the ISR photons are expected to be isolated from most other particles. These two photons are going to have an invariant mass equal to the π^0 mass at around $0.135\,\mathrm{GeV}$, which is relatively low assuming that we are dealing with high energy photons. In fact, even if photons did not originate from the same particle, if they are close to each other the invariant mass will generally be quite low compared to isolated photons. The higher energy photons will generally also have a higher invariant mass with other photons. However, the low energy of some photons might make the invariant mass of our high energy ISR photons very low, so we choose to calculate the invariant mass only with photons that have an energy of at least $500\,\mathrm{MeV}$. In order to improve the machine learning, we choose to have a pre-selection cut on $m_{\gamma\gamma}$, requiring it to be at least $0.25\,\mathrm{GeV}$. This value cut is based on observations of the invariant mass distributions between signal and background. This cut gives a signal efficiency of $\varepsilon_S = 0.703$ and a purity of $P = 0.0361$. We now move on to consider the training variables to select.

The ISR photons generally look distinct from other photons in the detector. If the transverse momentum of the ISR photon is very high, the expectation is that it is less likely that the e^+e^- annihilation occured in the first place. The angle between the photon and the electron beam $\theta_{\gamma,e}$ and its

Parameter	Description
$\theta_{\gamma e}$	Angle between the photon and the z-axis
$p_{t,jet}$	Transverse momentum of the nearest jet
$p_{t,e}$	Transverse momentum of the photon
$p_{\perp,jet}$	Momentum of the photon perpendicular to the nearest jet
$\theta_{\gamma,jet}$	Angle between the photon and the nearest jet
$m_{\gamma,\gamma}$	Smallest invariant mass between the photon and another photon
$m_{\gamma,ch}$	Smallest invariant mass between the photon and a charged particle

Table 6: Parameters used to distinguish between ISR photons and decay photons in the TMVA machine learning algorithms.

transverse momentum $p_{t,e}$ are both used as training parameters because for this reason. We generally expect the decay photons to originate from the original decay particles, meaning they should be close to the jets. We quantify distance from jets by the momentum of the photon perpendicular to the nearest jet $p_{\perp,jet}$ as well as the angle between the photon and the nearest jet $\theta_{\gamma,jet}$. Comparing the transverse momentum of the nearest jet $p_{t,jet}$ with the transverse momentum of the photon can also yield information about the photons. These three values related to the jet are all used as training parameters. Charged particles can radiate photons, so the invariant mass of the photon and its nearest charged particle $m_{\gamma,ch}$, as well as the the invariant mass of the photon with its nearest other photon above $0.5\,\text{GeV}$ are used as training variables.

Figure 14 shows a 2D histogram of these two parameters for ISR and decay photons. This graph shows the motivation behind using exactly $m_{\gamma,\gamma} = 0.25\,\text{GeV}$ as the preselection cut. A large chunk of decay photons have $m_{\gamma,\gamma}$ around 0 to $0.25\,\text{GeV}$ while the ISR photons are more randomly distributed, meaning a lot of background can be removed by this cut without sacrificing too many ISR photons. Appendix A shows plots that show how these 7 parameters differ between signal and background as well as how they relate to each other. Table 6 has an overview of every parameter used in the machine learning algorithm.

The ISR photons are trained on 7 different machine learning algorithms, Multidimensional likelihood estimator (PDERS), H-Matrix discriminant (HMa-
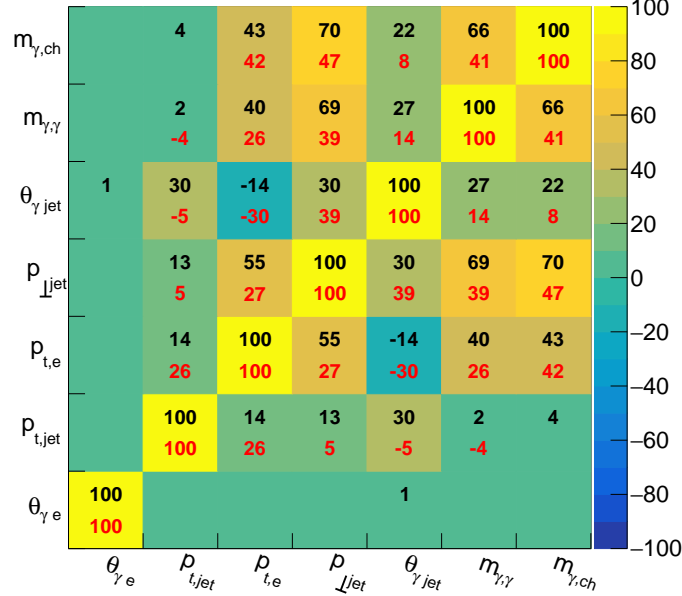
Figure 15: The Correlation matrix from the variables in table 6. The black numbers tell the correlation between the parameters for ISR while the red numbers tell the correlation between the parameters for normal photons. The colors are based on the ISR correlation matrix. Negative numbers means the parameters are anticorrelated. Many of the variables are correlated, but there is also a significant deviation in the correlation values from signal and background.

trix), Fisher discriminants (Fisher), BDT, Likelihood, KNN and Cuts. The details of these algorithms can be found in the TMVA user manual [20]. Similarly to the event selection, we plot a ROC curve to determine the difference in the efficiency between the algorithms. Figure 16 shows the background rejection as a function of signal efficiency for each algorithm. The ROC curve shows a larger background rejection for BDT in the range $\varepsilon_S = [0.1, 0.8]$ while Likelihood is higher for $\varepsilon_S = [0.8, 0.85]$. To know which range of signal efficiency we expect, optimize both methods for $\varepsilon_S \cdot P$. The optimization gives $\varepsilon_S \cdot P = 0.601 \cdot 0.533 = 0.32$ for BDT and $\varepsilon_S \cdot P = 0.581 \cdot 0.529 = 0.31$ for Likelihood, meaning BDT is better. We choose BDT as our classifier, giving us a signal efficiency of $\varepsilon_S = 0.601$ and purity of $P = 0.533$. The total signal efficieny for the entire ISR tagging now becomes $\varepsilon_S = 0.423$. This classification scheme is used to tag photons as ISR, which are removed from
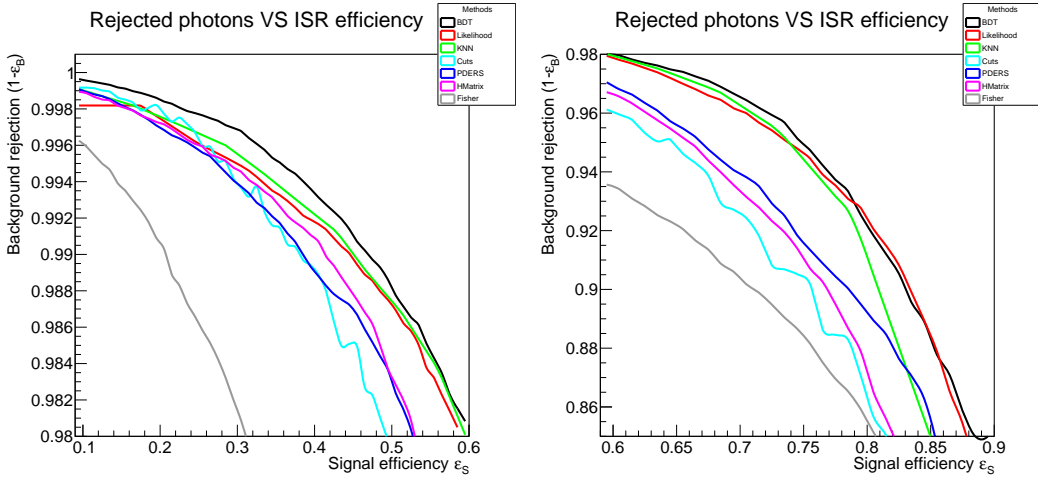
Figure 16: The rejected photons as a function of ISR efficiency for the seven tested machine learning algorithms. BDT has the highest background rejection for signal efficiencies between 0.10 and around 0.80, while likelihood is higher when between around 0.80 and 0.85.

the event and subtracting its 4-momentum from the total 4-momentum of the event $P = (0, 0, 0, \sqrt{s}) - p_{ISR}$.

The ISR tagging scheme was initially constructed on a data sample of $\sim$ 50000 semileptonic events. When the scheme was used on the $\sim$ 176000 signal and background sample events, we tagged 75 % less photons as ISR than we expected given the sample size. Closer investigations showed that the detection scheme for photons had been changed inbetween generation of the samples. Previously, the detector was set to never detect photons of energy less than $0.5\,\mathrm{GeV}$, but this cutoff had been lowered, among other possible changes. While that is unfortunate, both the training sample and the signal sample are simulations of particle physics at the FCC-ee. We will therefore hold on to the assumption that the ISR tagging scheme still holds up to the desired specifications.

Kinematic fitting

One of the main benefits of e^+e^- over pp collisions is the near complete knowledge of the initial state. In a hadronic collision, it is not known which partons of the proton were used in the collision or exactly how much energy was used in the collision. e^+e^- are different in that aspect, since the initial energy is completely focused on the electron positron pair, we know the

41

exact initial conditions of the event. There is still some difficulty, since inevitably some particles will be poorly measured or entirely lost, but the e^+e^- experiments have much better knowledge of the initial and final state of an event. Because of this knowledge of the event, we are able to perform a *kinematic fit*, a fit where we impose the physical laws governing the particle interactions on our event in order to improve our understanding of it. For example, we can demand that 4-momentum of the event is conserved and demand that certain particles together share an invariant mass equal to the mass of their mother particle. A kinematic fit where we impose physical conditions on the event is called a *constrained fit* and is the type of fit we shall use.

In a constrained fit, the underlying model for a system is expressed in the form of constraints

$$\vec{f}(\vec{a}, \vec{y}) = \begin{pmatrix} f_1(\vec{a}, \vec{y}) \\ f_2(\vec{a}, \vec{y}) \\ \vdots \\ f_m(\vec{a}, \vec{y}) \end{pmatrix} = \vec{0} \tag{52}$$

where $f_i(\vec{y})$ are the functions used to express constraints of the system, with $\vec{y}$ being the vector of n measurements and $\vec{a}$ is the vector of p parameters that the model depends on. The measurements will lie within some confidence region of the true underlying distribution, and they are unlikely to fulfil the conditions exactly, but corrections $\Delta\vec{y}$ can be added such that the conditions are fulfilled exactly by $\vec{y} + \Delta\vec{y}$.

The idea behind the constrained fit is to use the method of least squares [21] wherein we construct a function, χ^2, which measures the "cost" or difficulty of an event to satisfy our constraints and then minimize said function while preserving the constraints. There exists various ways to minimize a function subject to constraints. One very effective method is to use Lagrange multipliers and introduce a new function to be minimized

$$S(\vec{a}, \vec{y}) = \chi^2(\vec{y}) + 2\vec{\lambda} \cdot \vec{f}(\vec{a}, \vec{y}) \tag{53}$$

where $\vec{\lambda}$ are the Lagrange multipliers. The problem of minimising $S(\vec{a}, \vec{y})$ now reduces to a simultaneous solution of the equations

$$\frac{\partial S}{\partial \vec{y}} = \vec{0}, \quad \frac{\partial S}{\partial \vec{a}} = \vec{0}, \quad \frac{\partial S}{\partial \vec{\lambda}} = \vec{0} \tag{54}$$

We are interested in a parametrisation where χ^2 is quadratic in the parameters and thus can be written as

$$\chi^2(y) = \Delta\vec{y}^T \mathbf{V}^{-1} \Delta\vec{y} + g(x) \tag{55}$$

where $\Delta\vec{y}$ is the vector corrections to the measurements such that χ^2 obtains a minimum and $\mathbf{V}$ is the covariance matrix. Assuming the measurements are uncorrelated, the covariance matrix is a diagonal matrix

$$\mathbf{V} = \delta_{ij}\sigma_i\sigma_j \tag{56}$$

where σ_i is the resolution of the i-th measurement. We also allow for an additional function $g(x)$, which only depends on a scalar variable. This function is included such that it can take the form of a penalty function, which takes the form $g(x) = -2\ln(p(x))$, where $p(x)$ is a probability distribution function connected to the variables $\vec{y}$ via suitable constraints. Generally equations (54) is solved by iteration. In the special case where the problem is linear, it can be solved analytically. Nonlinear problems can be reduced to a set of linear problems by linearisation techniques and solved numerically. In order for the solution to converge the initial values should be given some thought. The initial values for $\vec{y}$ should be the measurements themselves, while the unmeasured parameters depend on the problem. For the semi leptonic case we have the unmeasured neutrino can be partially found using the missing 4-momentum. The issue with this approach is that the missing momentum is very dependent on the quality of the detection and the effects of the event reconstruction. The neutrino momentum cannot be reconstructed and must be kept as 3 free parameters, but using the missing 4-momentum is a reasonable initial value for the neutrino.

ABC-parametrisation

In the constrained fit the underlying parameters for the jets and leptons should be Gaussian distributed in order to ensure convergence of the fit. We choose to write a reconstructed jet as

$$\vec{p}_j^r = a_j|\vec{p}_j^m|\vec{p}_j^a + b_j\vec{p}_j^b + c_j\vec{p}_j^c \tag{57}$$

where the unit vectors $\vec{p}_j^{\,a}$, $\vec{p}_j^{\,b}$ and $\vec{p}_j^{\,c}$, are determined from the measured jet momentum and form a Cartesian system.

$$\vec{p}_j^{\,a} = \frac{\vec{p}_j^{\,m}}{|\vec{p}_j^{\,m}|}$$

$$\vec{p}_j^{\,b} = \frac{1}{\sqrt{p_{x,m}^2 + p_{y,m}^2}} \begin{pmatrix} p_{y,m} \\ p_{x,m} \\ 0 \end{pmatrix} \tag{58}$$

$$\vec{p}_j^{\,c} = \frac{1}{\sqrt{|\vec{p}_j^{\,m}|^2 (p_{x,m}^2 + p_{y,m}^2)}} \begin{pmatrix} -p_{x,m} p_{z,m} \\ -p_{y,m} p_{z,m} \\ p_{x,m}^2 + p_{y,m}^2 \end{pmatrix}$$

where $\vec{p}_j^{\,m}$ is the measured jet momentum. As can be seen, $\vec{p}_j^{\,a}$ follows the direction of the measured jet, $\vec{p}_j^{\,b}$ and $\vec{p}_j^{\,c}$ are defined to be orthogonal to the both $\vec{p}_j^{\,a}$ and each other. The initial values of the parameters are set to $a_j = 1$, $b_j = 0$, $c_j = 0$, so that the reconstructed particle vector initially is identical to the measured particle.

Performing a kinematic fit with `ABCfit++`

The `ABCfit++` software package was used and improved upon in order to perform a kinematic fit on our event samples. ABCfit was originally developed by Oliver Buchmuller and Jørgen Beck Hansen. It was then converted to `C++` by Julie Torndal. In `ABCfit++`, the constrained fit supports constraints with a probability distributed function. This in necessary in order to perform constraints on the masses of particles due to the particles being highly unstable and have a Breit-Wigner resonance. The particles are therefore not expected to be exactly on resonance. The fit handles this by incorporating the distribution functions into the penalty function $g(x)$. The details of how `ABCfit++` performs its fit can be found on [13]. As part of this thesis, the speed of computations with `ABCfit++` was optimized make fits with more constraints more feasible.

In our constrained fit, we will be imposing 4-momentum conservation

$$\sum_{i=1}^{N} \vec{p}_i = \vec{0}, \qquad \sum_{i=1}^{N} E_i = 365 \, \text{GeV} \tag{59}$$

as well as Gaussian distributed masses of the W boson and the top particle

$$\mu_W = 80.5 \, \text{GeV}, \quad \sigma_W = 2.1 \, \text{GeV} \quad \mu_t = 173 \, \text{GeV}, \quad \sigma_t = 1.5 \, \text{GeV} \tag{60}$$

the standard deviations of the masses are loosely based on a mix between the measured standard deviation and the standard deviation from the invariant mass distribution jets that were matched to the top quark decay. It is generally better to be more lenient with the standard deviations, since jets are rarely measured perfectly and particles can be lost in the detector hole. Imposing these conditions means that we have 8 constraints that has to be satisfied.

Using these constraints in `ABCfit`, we can perform a kinematic fit on our events. When doing so we assign each jet to the quark that produced it. One jet is assigned to the bottom quark whose sister decay W boson decayed into a lepton neutrino pair, one jet is assigned to the other bottom quark and the last two jets are both assigned as indistinguishable light quark jets. The high energy lepton is assigned as the lepton and the missing momentum is assigned to the neutrino as an unmeasured particle. This gives a total of 12 different combinations of assigning jets. In order to find the correct combination we perform the kinematic fit for each of the 12 combinations on each event and use equation (55) to calculate their χ^2 value. Then we take the combinations that returned the lowest value and keep the corrections returned by the fit. The initial covariance matrices used for the leptons, b-jets and light quark jets are the default values in the software package for semileptonic events. They are

$$
\begin{aligned}
V_{lepton} &= \mathrm{diag}(0.003, 0.003, 0.003, 10) \\
V_{b-jet} &= \mathrm{diag}(0.07, 1.2, 1.2, 10) \\
V_{lq-jet} &= \mathrm{diag}(0.07, 1.4, 1.4, 10)
\end{aligned}
\tag{61}
$$

the fourth element of the matrix is the resolution of d, the mass resolution and is not used for the fit since instead the mass parameter is kept fixed after rescaling the energy and momentum of the input particles to have zero mass. The default covariant matrix values were originally chosen by performing a kinematic fit on semileptonic events with 6 constraints and measuring the standard deviation of the distributions, so they might differ from events with 8 constraints. When the kinematic fit is performed on our selected events, the photons tagged with the ISR photons are removed from the event beforehand to improve the fit.

Analysis

Determination of Anomalous contributions/couplings

When the SMEFT terms were initially introduced, we observed from equation (47) that the anomalous coupling matrix elements has a parabolic dependence for variations of a single anomalous coupling constant α. This parabola we can be determined from three of its points. By performing three simulations for three different values of the anomalous coupling constant α, we can use the signal data to find the parabola in equation (47). Since the SM has no anomalous couplings it is equivalent to $\alpha = 0$. By simulating events with model parameters of two different values, say $\alpha = 1$ and $\alpha = -1$, we are able to construct the parabola associated with the anomalous coupling constant. For each free parameter we simulate $e^+e^- \to t\bar{t}$ events with the parameter set to either $+1$ or -1, except the vl_tbW_Re, which is varied by ±0.5. Calculating the cross section of these events using `Whizard` we can calculate the expected amount of events, which determines the size of our simulated samples. Table 7 shows the values of the parameters that were used for simulation, the associated cross section and the amount of events simulated for each value of the parameters.

Generally the cross sections of the `Whizard` simulations are a higher than that of the `Pythia` simulations. There can be many reasons for this, but a large contributor is that our `Whizard` simulations are without ISR. The solution is not so simple as just enabling ISR in our `Whizard` simulations, since `Whizard` and `Pythia` handles ISR in vastly different ways. Calculating the cross sections of the `Whizard` simulations with ISR enabled reduces the cross section of the SM top pair production to $\sigma = 0.368$pb, which is much lower than our `Pythia` cross section of $\sigma = 0.452$pb. The cross section for the anomalous couplings are reduced in a similar way with the cross section being approximately reduced by a factor 0.76 when enabling ISR.

Observables

In this analysis the observables investigated are the cross section and angular distributions. There are a total of 5 angles of interest, one for the $e^+e^- \to t\bar{t}$ interaction, and two each for the $t \to Wb$ and $W \to l\nu$ interactions. The first angle is the polar angle between the electron-beam and the reconstructed top particle which is given by

$$\cos\theta_{et} = \frac{\mathbf{p}_e \cdot \mathbf{p}_t}{|\mathbf{p}_e||\mathbf{p}_t|} \tag{62}$$

Parameter	Value	σ[fb]	$N_{Expected}$
SM	0	483.36486 ± 0.00881	725047
vl_tbW_Re	+0.5	830.76864 ± 0.0198	1246095
	-0.5	445.32765 ± 0.00117	667990
vr_tbW_Re	+1.0	483.36919 ± 0.00883	725053
	-1.0	483.36758 ± 0.00971	725047
tl_tbW_Re	+1.0	483.37136 ± 0.00895	725050
	-1.0	483.37002 ± 0.00903	725068
tr_tbW_Re	+1.0	2590.9401 ± 0.00707	3886404
	-1.0	4129.1537 ± 0.0137	6193785
tv_ttA	+1.0	2874.0235 ± 0.0157	4311045
	-1.0	7415.8362 ± 0.0320	11123775
ta_ttA	+1.0	650.49347 ± 0.0132	975750
	-1.0	650.51152 ± 0.0130	975735
vr_ttZ	+1.0	790.68660 ± 0.00204	1186029
	-1.0	485.36979 ± 0.0159	728055

Table 7: The model parameters values used in simulations, the resulting `Whizard` cross section and expected amount of events. The expected events were found by multiplying the cross section with the expected luminosity of $\mathcal{L} = 1.5\text{ab}^{-1}$.

where $\mathbf{p}_t$ is the momentum of the top particle and $\mathbf{p}_e$ is the vector of the electron beam. Since we are only interested in the angle, we choose this to be a unit vector along the z-axis $\mathbf{p}_e = \hat{\mathbf{z}}$. The second and third angle of interest is the polar and azimuthal angle between the top product and its decay product. The polar angle between a particle and its decay product can be calculated by boosting the reference frame from the laboratory frame to that of the top particle. In order to simplify this transformation we decompose the decay product momentum into components parallel and orthogonal to the mother particle. These components are calculated from

$$\mathbf{p}_{d\parallel} = (\mathbf{p}_m \cdot \mathbf{p}_d)\frac{\mathbf{p}_m}{(\mathbf{p}_m)^2} \tag{63}$$

$$\mathbf{p}_{d\perp} = \mathbf{p}_d - \mathbf{p}_{d\parallel} \tag{64}$$

47

where $\mathbf{p}_m$ is the mother particle and $\mathbf{p}_d$ is the daughter particle. The parallel component tranforms by

$$\mathbf{p}_{d\parallel}^* = \gamma(\mathbf{p}_{d\parallel} - \beta E) \tag{65}$$

where $\gamma = \frac{1}{\sqrt{1-\beta^2}}$ is the Lorentz factor and E is the energy of the mother particle. We can now find the polar and azimuthal angles. The polar angle between a particle and its decay product is given by

$$\cos\theta_{md}^* = \frac{\mathbf{p}_{d\parallel}^*}{\sqrt{(\mathbf{p}_{d\parallel}^*)^2 + (\mathbf{p}_{d\perp})^2}} \cdot \frac{\mathbf{p}_m}{|\mathbf{p}_m|} \tag{66}$$

In the reference frame of the mother particle, the z-axis lies parallel to its flight direction with $\hat{\mathbf{z}}' = \frac{\mathbf{p}_m}{|\mathbf{p}_m|}$. Using this reference frame, the decay product can be decomposed into x' and y' and used to calculated the azimuthal angle. The x'-axis is found by taking the cross product between $\hat{\mathbf{z}}'$ and the $\hat{\mathbf{z}}$, giving $\mathbf{x}' = \hat{\mathbf{z}}' \times \mathbf{p}_e$. Then we find $\mathbf{y}'$ by taking the cross product of the two other vectors $\mathbf{y}' = \mathbf{x}' \times \hat{\mathbf{z}}'$. $\mathbf{x}'$ and $\mathbf{y}'$ are not unit vectors, but they point in the directions of the x'-axis and y'-axis and have the same length $|\mathbf{x}'| = |\mathbf{y}'| = |\sin\theta_{et}|$, they cancel when the azimuthal angle is calculated by

$$\phi_{md}^* = \arctan\frac{\hat{\mathbf{x}}' \cdot \mathbf{p}_d}{\hat{\mathbf{y}}' \cdot \mathbf{p}_d} \tag{67}$$

One issue from this approach is that the arctan function only gives values in the range $\phi \in (-\pi/2, \pi/2)$, but we want values in the range $(-\pi, \pi)$. In order to fix this, we need to extract extra information from the decomposition of the decay product momentum. If the true azimuthal angle is between $-\pi/2$ and $\pi/2$, then the function works fine. But since $\tan(\phi + \pi) = \tan(\phi)$, when the true angle is in the range $[\pi/2, \pi]$ we get an angle of $\phi \in (-\pi/2, 0]$. Similarly, when the true angle is in the range $[-\pi, \pi/2]$, we get $\phi \in [0, \pi/2)$. This means if the x component is negative a factor π is either added or subtracted, depending on the sign of the y-component. The new formula for the true azimuthal angle is thus

$$\phi_{md}^* = \arctan\frac{\hat{\mathbf{x}}' \cdot \mathbf{p}_d}{\hat{\mathbf{y}}' \cdot \mathbf{p}_d} + \frac{1}{2}\text{sgn}\,(\hat{\mathbf{y}}' \cdot \mathbf{p}_d)(1 + \text{sgn}\,(\hat{\mathbf{x}}' \cdot \mathbf{p}_d))\pi \tag{68}$$

Systematic effects from the event selection

With the event selection and reconstruction completed we have our final event sample with our vastly improved purity of $P = 0.923$, but with a signal efficiency of $\varepsilon_S = 0.565$, nearly 44 % of signal events were lost. We would therefore like to understand if the signal efficiency is constant over the range of observables. We examine this by comparing the angular distributions before and after the event selection. Most of the lost events were due to being unable to detect or identify the lepton, meaning the events removed by preselection cuts were mainly due to them containing W bosons that decayed into taus, which then decayed hadronically. By examining angular distributions of the simulated quark level particles before and after the event selection, we can examine how the distribution changes. Figure 17 shows the normalized distributions of $\cos(\theta_{et})$, θ_{tb}^* and ϕ_{tb}^* for events before and after the event selection. Examining the plots closer it seems that there is not much difference. To quantify the effect we can perform a Kolmogorov-Smirnov (KS) test.

A KS test is a test on the equality of two one-dimensional distributions which can be used to either compare a sample to a analytical distribution or to compare two samples. The two sample KS test gives a probability that two samples were drawn from the same distribution by converting the samples into Empirical Distribution Functions (EDFs). In laymans terms, an EDF is a numerical estimation of a Cumulative Distribution Function (CDF) that approaches the true CDF with larger and larger sample sizes. The KS test measures the largest difference between the two EDFs and used it to get a probability that the two samples came from the same probability distribution. We will be using a KS test to compare our two samples, before and after event selection. `ROOT` has a built-in function that can perform a KS test on two distributions. The more bins in a histogram, i.e. the higher the resolution, the better the KS test will work, so using the `ROOT` functionality we perform a KS test on the distributions with 100 bins then re-bin the histograms to get the plots in figure 17. The KS test on $\cos(\theta_{et})$ yields a p-value of exactly 1, θ_{tb}^* yields a p-value of $1.6 \cdot 10^{-3}$ and ϕ_{tb}^* yields a p-value of 0.94. Both $\cos(\theta_{et})$ and ϕ_{tb}^* have high p-values indicating that the distributions are almost completely unaffected by the event selection. Meanwhile the very low p-value of θ_{tb}^* indicates that the event selection, either the preselection or TMVA, causes systematic errors to our sample.

The signal efficiency is not guaranteed to be equal for all the anomalous couplings. Figure 18 shows the efficiency for all the couplings as well as for the SM. The efficiency is higher for the couplings by about 1 % except for the tr_tbW_Re model parameter, which corresponds to the δg_R coupling, which

gives a lower signal efficiency by about 1 %. The plot has been made to fit to a parabola since the observable effects of the anomalous coupling constants have been shown to be parabolic. The efficiencies for two opposite values of the coupling are similar, indicating that the SM is the parabola's extremum.

Results

After the event selection, the constrained fitting technique is applied to our signal, background and anomalous coupling events. We perform the fit with 8 constraints given by equations (59) and (60) with 3 free parameters in the form of the neutrino momentum, which is given the missing 4-momentum as its initial values. The fit gives us the reconstructed jets, leptons and neutrino, their a, b and c parameters, the lepton charge and which quarks are associated with which jets. Figures 19 and 20 show the distributions of the a, b and c parameters for the leptonic b-jets, hadronic b-jets, light flavour jets and leptons. The values from the covariant matrices from equation (61) were found from the standard deviations of the ABC distributions for constrained fits with 6 parameters. Said constrained fit thus did not distinguish between b-jets, giving the same covariant matrix to both of them.

In the constrained fit for 8 parameters, the observed resolution of a for the leptons is 0.04, for leptonic b-jets 0.17, hadronic b-jets 0.18 and light quark jets 0.19. The b and c parameter resolutions are equal for each object, with them being 0.0006, 0.14, 0.17 and 0.21 for the leptons, leptonic b-jets, hadronic b-jets and light quark jets, respectively. `ABCfit++` also changes the parametrisation of the jets $(a, b, c) = (1.03, 0, 0)$ due to the mean of the jet a distributions being 1.03. In our case we get that the mean of a is 1.07 for the leptonic b-jets, 1.06 for hadronic b-jet and 1.01 for the light quark jets. These values differ from the ones found from a fit with 6 constraints used in the covariant matrices in equation (61) and interestingly gives differing resolutions for leptonic and hadronic b-jets, with the leptonic b-jets being lower in standard deviations but higher in mean. This is likely due to the effects of the neutrino. The leptonic b-jet constraints are mostly dependent on the unmeasured neutrino, which the fit can vary freely instead of varying the b-jet.
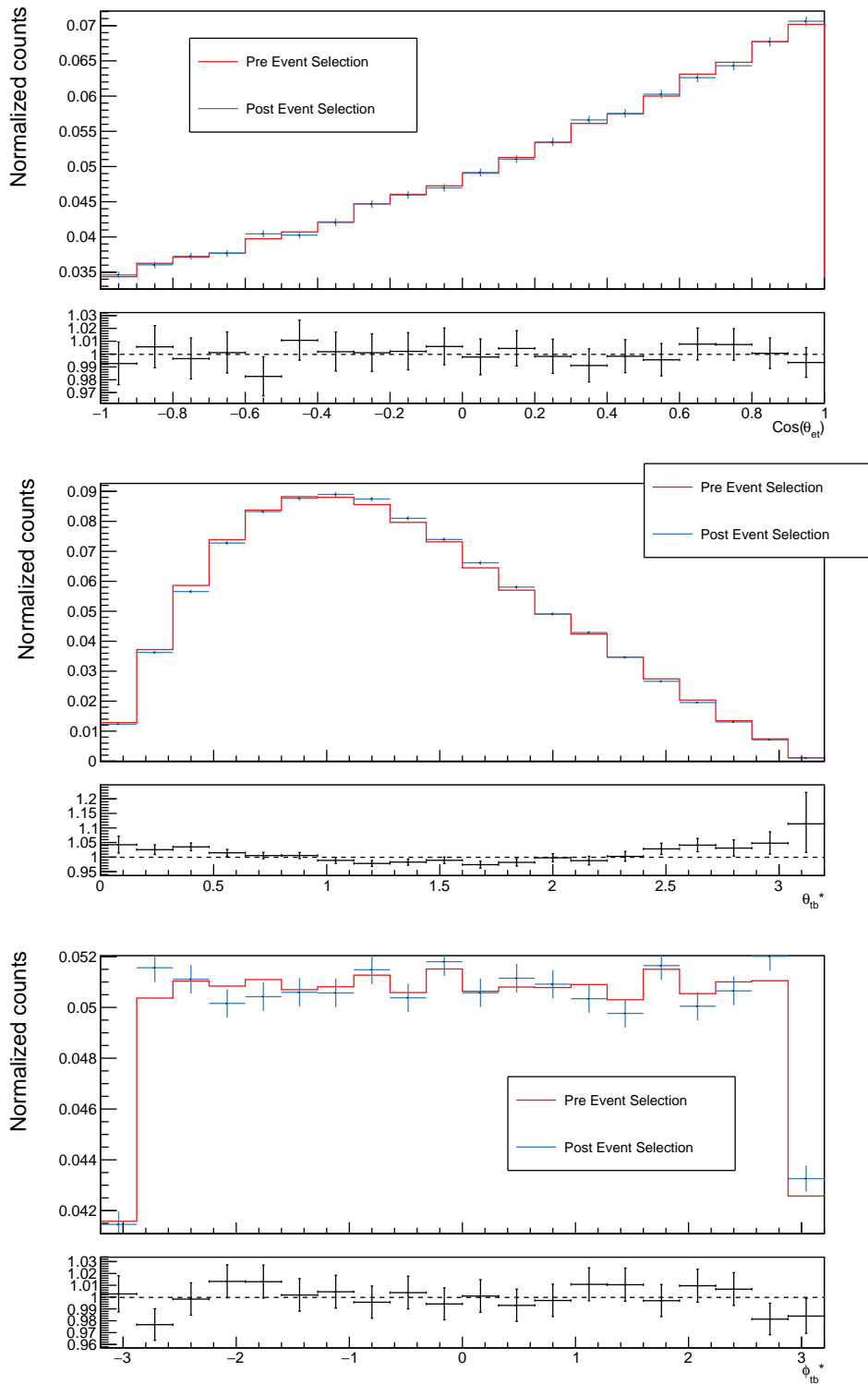
Figure 17: Normalized distributions of $\cos(\theta_{et})$, θ_{tb}^* and ϕ_{tb} before and after the event selection.
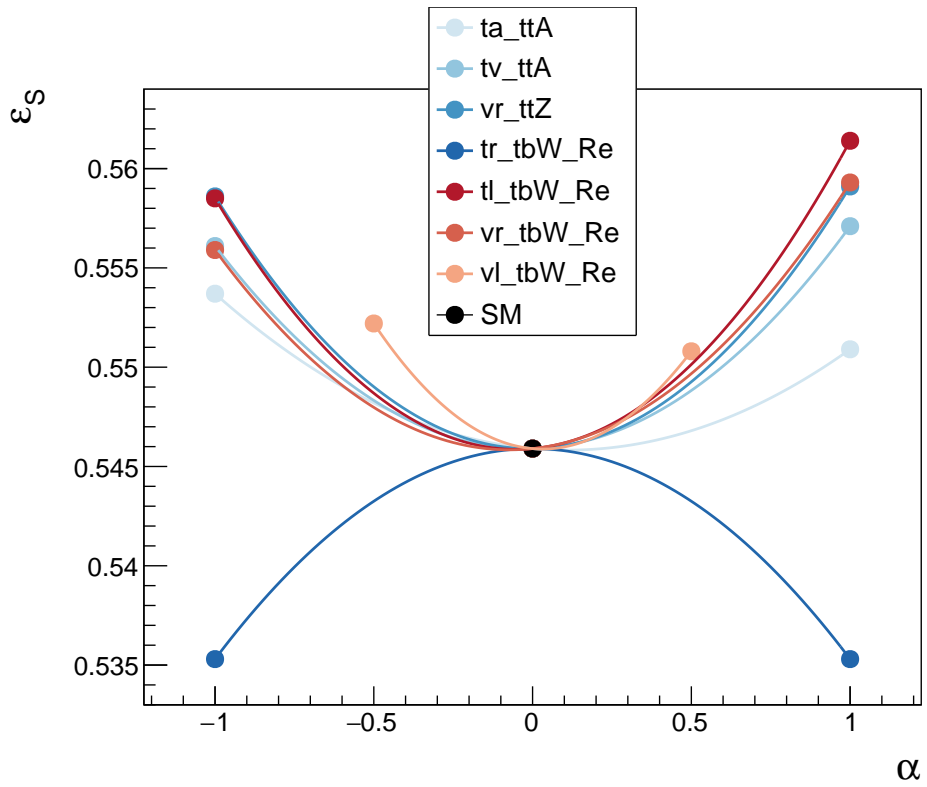
Figure 18: Efficiency of event selection for all couplings and the Standard Model.
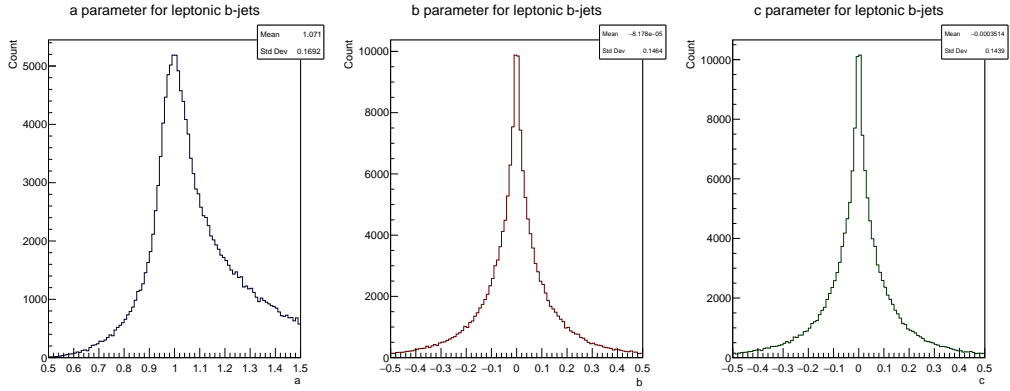
(a) a,b and c parameter distributions for leptonic b-jets.
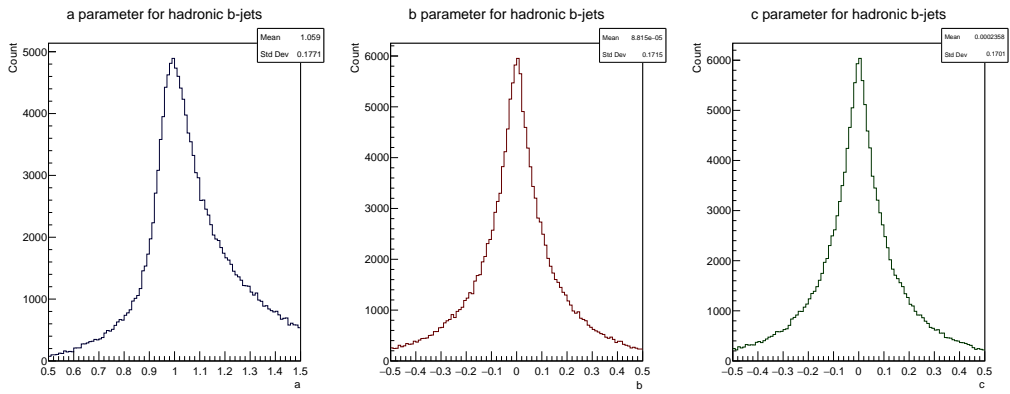
(b) a,b and c parameter distributions for hadronic b-jets.
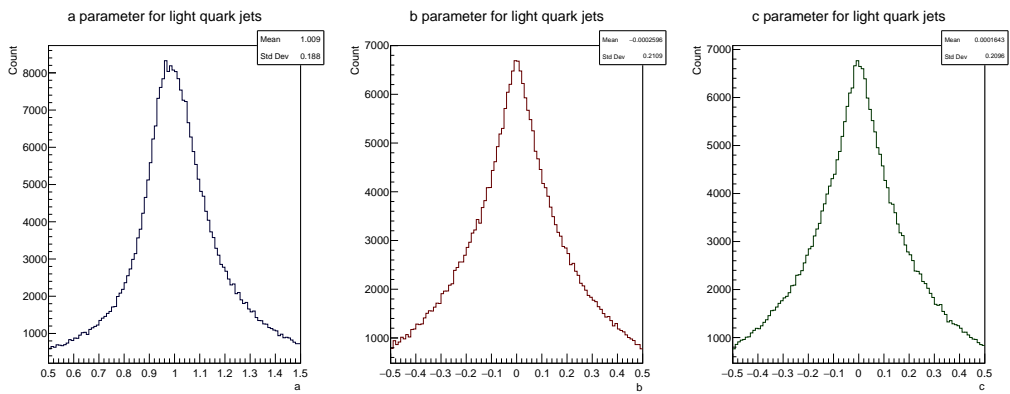
(c) a,b and c parameter distributions for light quark jets.

Figure 19

53
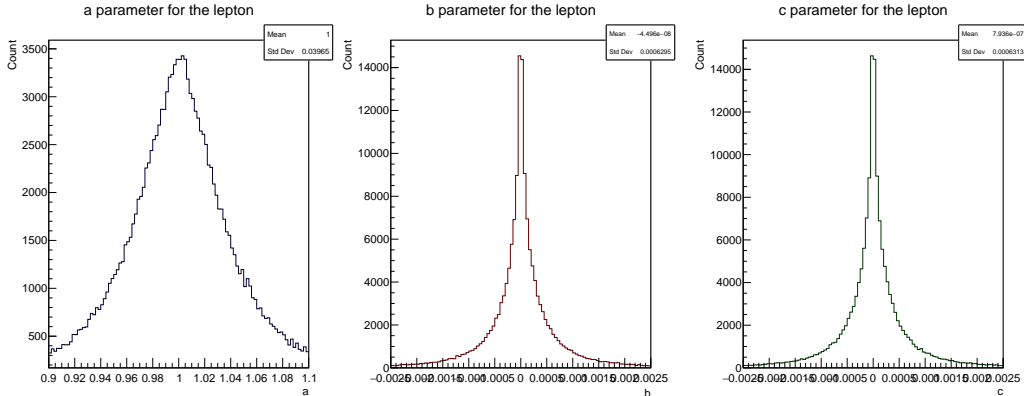
Figure 20: a,b and c parameter distributions for leptons.

After the constrained fit has been completed we are left with a reconstruction of the original 6 objects of the semileptonic $t\bar{t}$ process, the $b\bar{b}$ pair, the lepton neutrio pair and the light quark pair. Using 4-momentum conservation we can reconstruct the original $t\bar{t}$ pair and W^+W^- pair and we can distinguish between particle and antiparticle by the charge of the lepton. From these reconstructed particles, we can calculate the angles.

It follows quite intuitively that if the anomalous couplings are extremely small, the variation from the SM is so small that it is nearly impossible to detect. Correspondingly if the couplings are extremely large, we could easily detect the variation. This means that if we know the contribution to the observables as a function of the coupling value, we can construct a confidence interval on the coupling which can provide some insight into the FCC-ee sensitivity to the anomalous coupling terms. As seen previously, the anomalous coupling matrix elements has a parabolic dependence for variations of a single coupling parameter α. For any parabola $Ax^2 + Bx + C$ the A, B and C parameters can be determined from three of its points. We have three different samples for three different values of the model parameters $\{\alpha^+, \alpha^0, \alpha^-\}$, with $\alpha^0 = 0$ being the SM parameter value. Using these three points we can construct the parabola from equation (47) and find the full function f that describes the contribution of the anomalous couplings as a function of its value α. Using this technique we get

$$
\begin{aligned}
f(\alpha^0) &= C \\
f(\alpha^+) &= A\alpha^2 + B\alpha + C \\
f(\alpha^-) &= A\alpha^2 - B\alpha + C
\end{aligned}
\tag{69}
$$

where $f(\alpha)$ is one of the angular distributions. The parameters can thus be

determined

$$
\begin{aligned}
A &= \frac{f(\alpha^+) + f(\alpha^-)}{2\alpha^2} - \frac{f(SM)}{\alpha^2} \\
B &= \frac{f(\alpha^+) - f(\alpha^-)}{2\alpha^2} \\
C &= f(SM)
\end{aligned}
\tag{70}
$$

Including the background the fit model becomes

$$
f(\alpha) = A \cdot \alpha^2 + B \cdot \alpha + f(SM) + f(Bkg)
\tag{71}
$$

By using this technique on each bin of three histograms of the same angular distribution at the three values $(\alpha^+, \alpha^0, \alpha^-)$, a function $f_i(\alpha)$ for each bin can be acquired. Now that we have the functions associated with the anomalous couplings, we can find the confidence intervals. The confidence intervals are determined by using a least-squares method where the histograms of the signal region are fitted to the model above. The χ^2 is calculated from the sum of bin

$$
\chi^2 = \sum_{i=1}^{n} \frac{(y_i - f_i(\alpha))^2}{\sigma_{y_i}^2 + \sigma_{f_i(\alpha)}^2}
\tag{72}
$$

where the numerator is the square of the difference in the bin content between the signal region histogram and the fit model for the ith bin and the denominator is the square of the error of the difference found from error propagation. According to Poisson statistics, the error on each bin is the square root of the bin content. In order to get the errors for the histograms we simply square the bin content of the sum of the signal and background histograms. Since the `Whizard` cross sections from table 7 are slightly higher than the `Pythia` cross sections, the `Whizard` angular distributions have been scaled with a factor $\frac{0.452}{0.4834} = 0.935$ to compensate for the difference. Figure 21 shows the angular distributions of the semileptonic events for the values $\alpha = -1, 0, 1$ of the `Whizard` parameter ta_ttA, while figure 22 shows the associated 1σ fit. Figures 23-26 shows the fit for the other angular distributions of the ta_ttA parameter. The fit figures for the other parameters can be found in Appendix B. The left side shows the χ^2 fit with the The right side shows how the fit data coincided with the fit model.
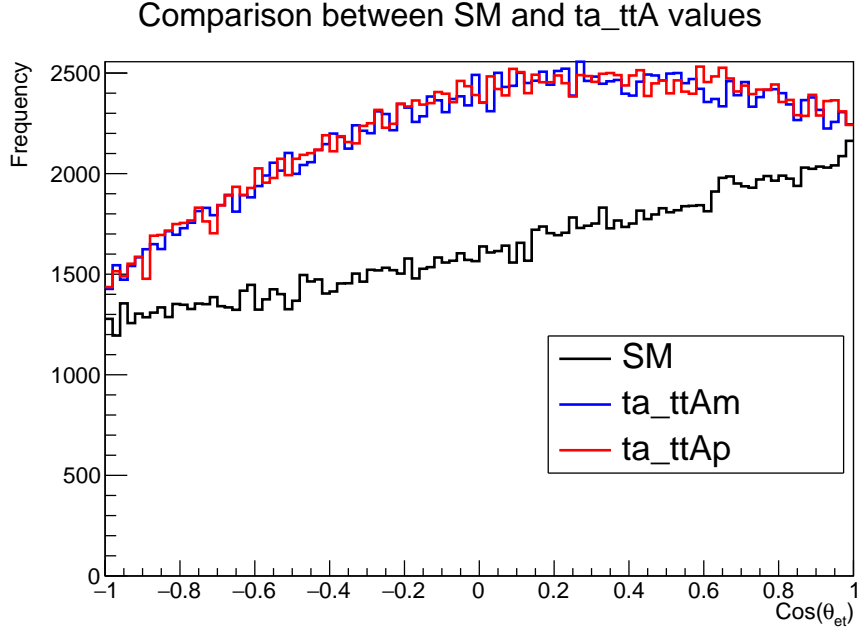
Figure 21: $\cos\theta_{et}$ for different values of ta_ttA. The p or m suffix corresponds to positive or negative coupling values. As can be seen the higher cross section of ta_ttA creates a higher amount of events. The shape is also different, which is expected since the ta_ttA term affect the $\gamma \to t\bar{t}$ vertex.
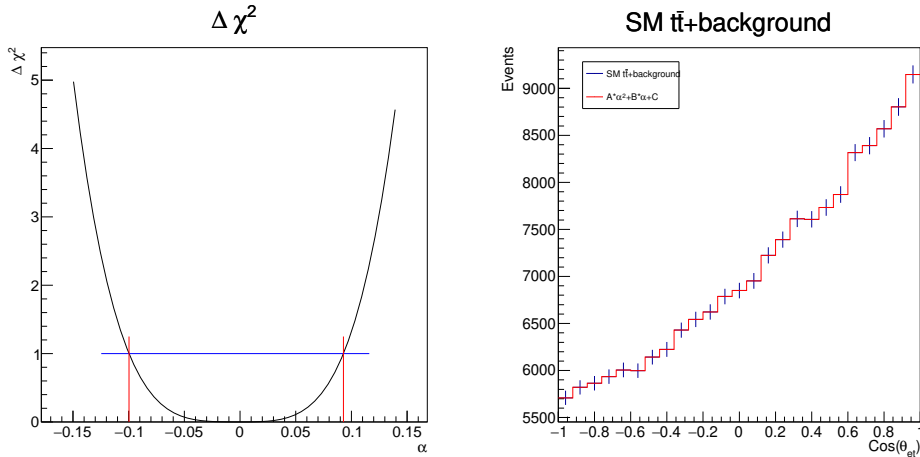
Figure 22: The $\cos\theta_{et}$ fit for ta_ttA.
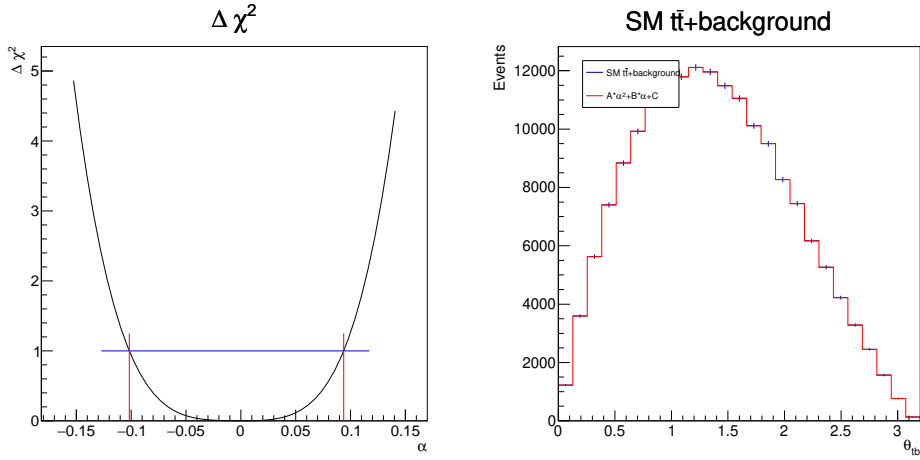
Figure 23: The θ_{tb}^* fit for ta_ttA.
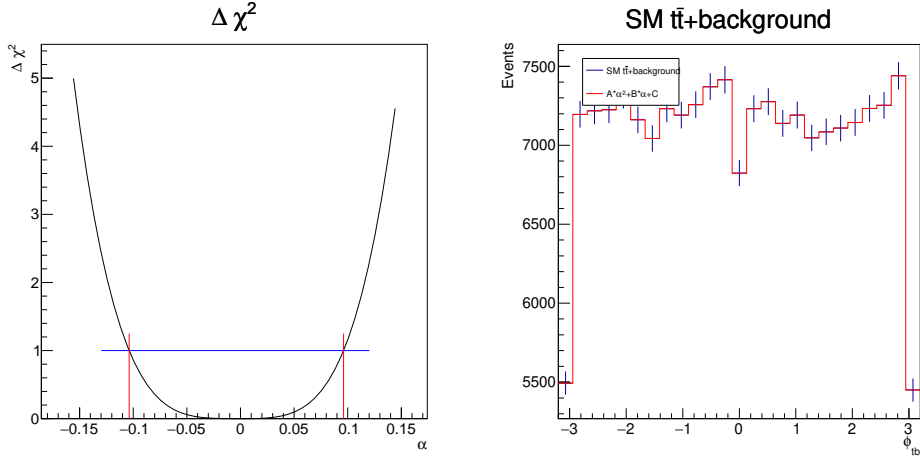
Figure 24: The ϕ_{tb}^* fit for ta_ttA.
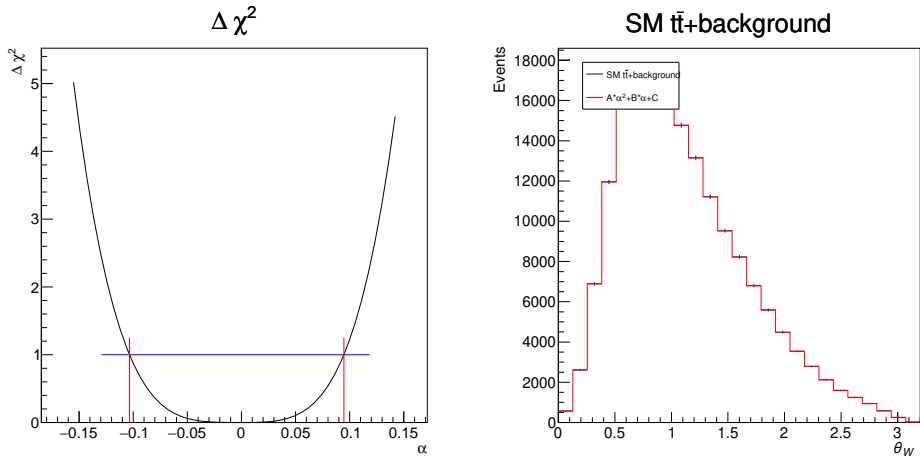
Figure 25: The θ_{Wl}^* fit for ta_ttA.
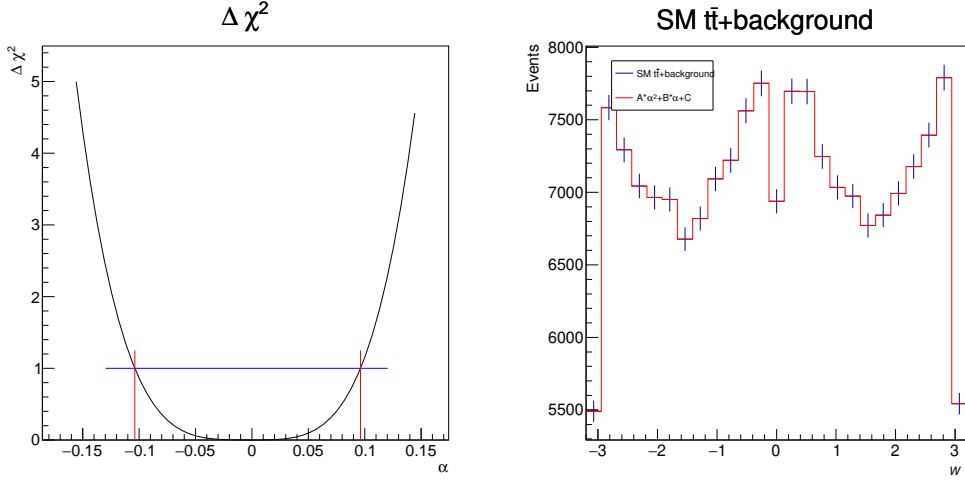
Figure 26: The ϕ^*_{Wl} fit for ta_ttA.

Table 8 shows the final results in the form of the 35 1σ confidence intervals for the anomalous coupling constants. The anomalous coupling terms with high cross sections show a much smaller confidence interval than couplings with cross sections comparable to the SM. The cross sections for the couplings can be shown is table (7). The tv_ttA and tr_tbW_Re coupling parameters have the two the highest cross sections and the lowest confidence intervals of the parameters. This behaviour is to be expected since a higher cross section will give unexpectedly high amounts of signal events. Couplings vl_tbW_Re and vr_ttZ also have smaller confidence intervals, possibly due to the large difference in cross section between the parameter values. Couplings vr_tbW_Re and tl_tbW_Re have relatively large confidence intervals due to the similarity of their cross sections to that of the SM.

It is important to consider the changes in signal efficiency when different coupling parameters are enabled. Since the main sensitivity to the couplings comes from how they affect the cross section, the fact that the efficiency changes at the same time means we will have an additional uncertainty when measuring our confidence interval. Figure 18 demonstrates the efficiency deviations from the SM for each of the couplings. For couplings with a cross section higher than the SM, a higher efficiency will cause a smaller confidence interval and a lower efficiency will cause a large confidence interval. This means that for an event selection with equal efficiency for all the couplings, the tr_tbW_Re term is expected to actually have a smaller confidence interval than the one given.

58

Coupling	θ_{et}	θ_{tb}^*	ϕ_{tb}^*	θ_{Wl}^*	ϕ_{Wl}^*
vl_tbW_Re	[−0.004637, 0.00457]	[−0.004511, 0.004445]	[−0.00462, 0.004551]	[−0.004517, 0.004451]	[−0.004624, 0.004554]
vr_tbW_Re	[−0.3059, 0.3739]	[−0.2905, 0.3732]	[−0.2878, 0.3367]	[−0.1078, 0.1253]	[−0.2691, 0.4068]
tl_tbW_Re	[−0.2788, 0.2999]	[−0.2549, 0.2926]	[−0.2635, 0.3109]	[−0.06984, 0.07071]	[−0.2892, 0.3139]
tr_tbW_Re	[−0.00237, 0.002413]	[−0.002318, 0.002359]	[−0.002353, 0.002395]	[−0.002236, 0.002275]	[−0.002355, 0.002397]
ta_ttA	[−0.09968, 0.09284]	[−0.1017, 0.09378]	[−0.1038, 0.09615]	[−0.1035, 0.09468]	[−0.1038, 0.09626]
tv_ttA	[−0.0007738, 0.0007763]	[−0.0007593, 0.0007617]	[−0.000771, 0.0007734]	[−0.0007589, 0.0007613]	[−0.0007708, 0.0007732]
vr_ttZ	[−0.009407, 0.00926]	[−0.01143, 0.01115]	[−0.01161, 0.01133]	[−0.01144, 0.01116]	[−0.01163, 0.01135]

Table 8: The 1σ confidence intervals of α for each coupling and angle of interest.

Conclusion

From the analysis the expected sensitivity of the FCC-ee to the anomalous top couplings was determined and characterized by 1σ confidence intervals shown in table 8. These confidence intervals were constructed through a least squares fit for each coupling and angular distribution by comparing a fit function to the angular distribution of the SM sample events. The fit function is a parabola and was determined for each angle and coupling from three angular distributions at three different values of the same coupling. The SM samples are obtained by simulating $t\bar{t}$ pair production through the semileptonic decay channel and associated background events at the FCC-ee at $\sqrt{s} = 365$. Using the framework of `FCCSW`, a fast simulation of the experimental environment of the IDEA detector was performed on the simulated events before reconstruction.

An event selection was performed partly by manual cuts and partly by machine learning. The initial manual cut both improves the machine learning selection and ensures the ability to reconstruct the semileptonic $t\bar{t}$ event. A variety of machine learning algorithms were examined before using the Boosted Decision Tree algorithm. The trained algorithm had a signal efficiency of $\varepsilon_S = 0.965$ while the signal efficiency of the manual cuts were $\varepsilon_S = 0.565$, giving a total signal efficiency of $\varepsilon_S = 0.548$ with a purity of $P = 0.9225$. After the event selection initial state radiation is taken into account by attempting to tag ISR photons through machine learning algorithms. A two manual cuts were performed before using the BDT algorithm to tag photons as ISR.

Once ISR has been tagged and removed from the event, the event is reconstructed using a constrained fit. The constrained fit was performed using the `ABCfit++` software package to obtain a reconstruction of the original decay particles whose angular distributions are examined and fitted to the parabolic fit function. The anomalous coupling confidence intervals show that even small variations of the couplings could be observed at the FCC-ee and offers a fast way to either confirm or deny certain beyond the standard model physics provided the FCC-ee lives up to its specifications.

As part of this study functionalities were developed for the `FCCAnalyses` framework and improvements were made to optimize the speed of `ABCfit++`. This thesis hopefully serves as a stepping stone for more sophisticated investations of the anomalous couplings. As the FCC-ee project progresses, new software developments and more information about the kinematics can be taken into account for future studies and can hopefully improve on the sensitivity reach and accuracy of this study.

Appendix A: ISR plots
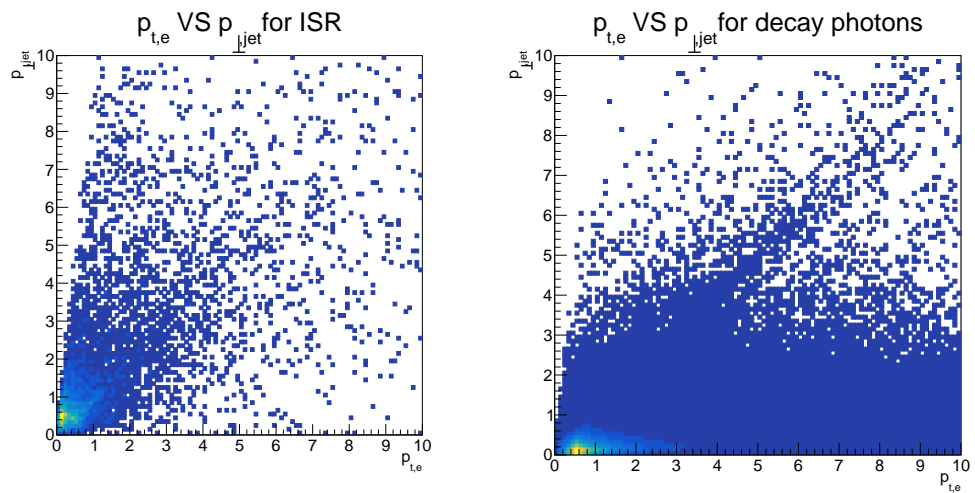
Figure A.1: p_t VS momentum perpendicular to nearest jet for ISR (left) and decay photons (right).
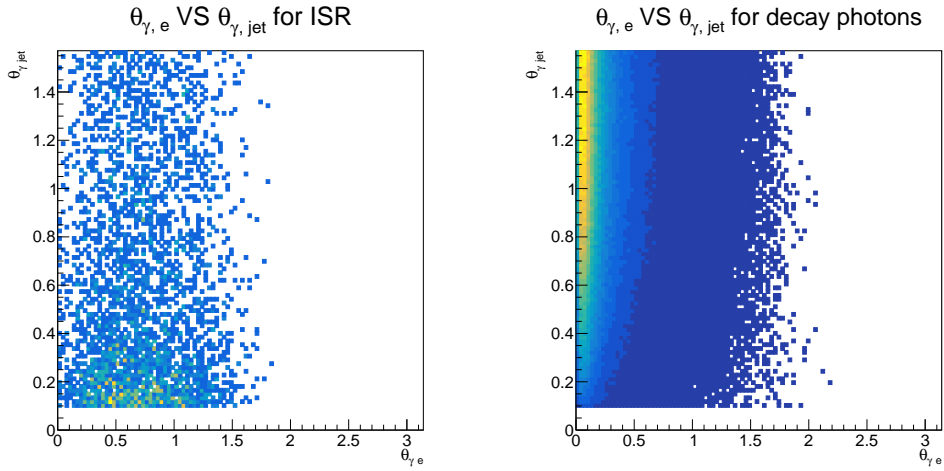
Figure A.2: Angle to nearest jet VS angle to the z-axis for ISR (left) and decay photons (right).
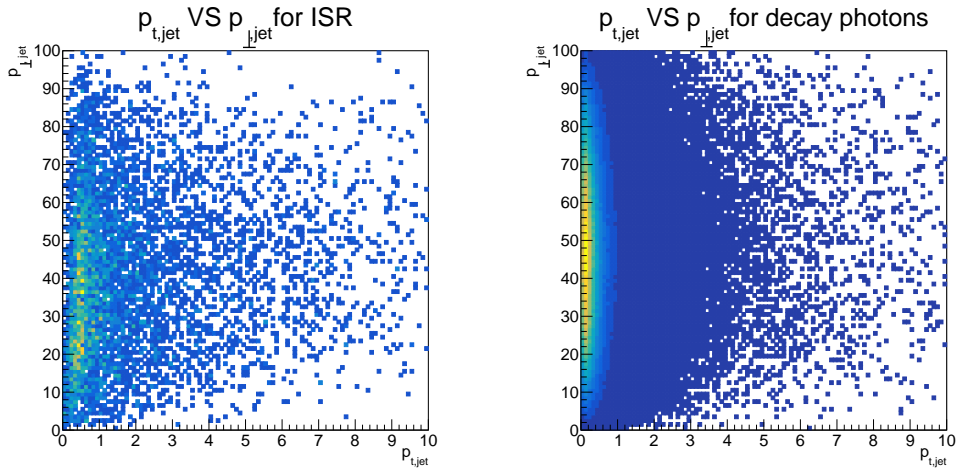
Figure A.3: p_t for the nearest jet VS momentum perpendicular to nearest jet for ISR (left) and decay photons (right).

Appendix B: Fits on the couplings

vl_tbW_Re
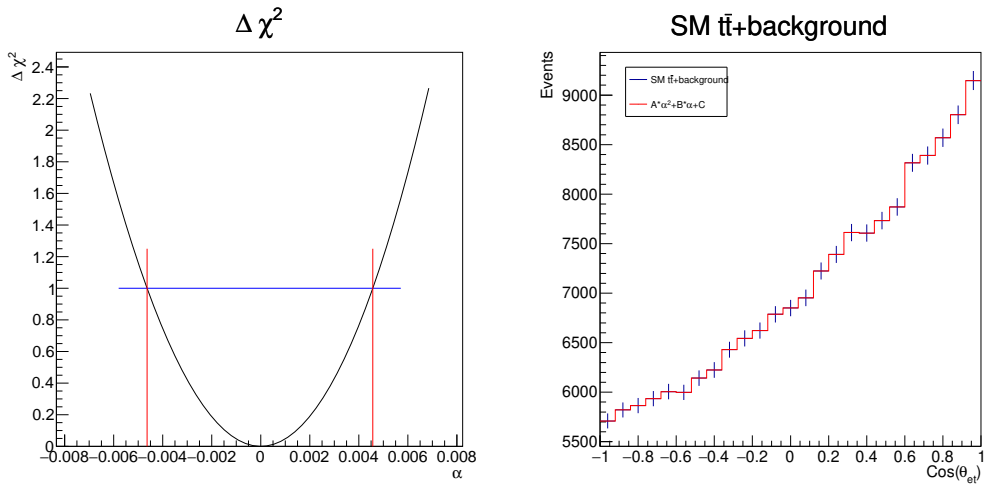
Figure B.1: $\cos\theta_{et}$ for vl_tbW_Re.
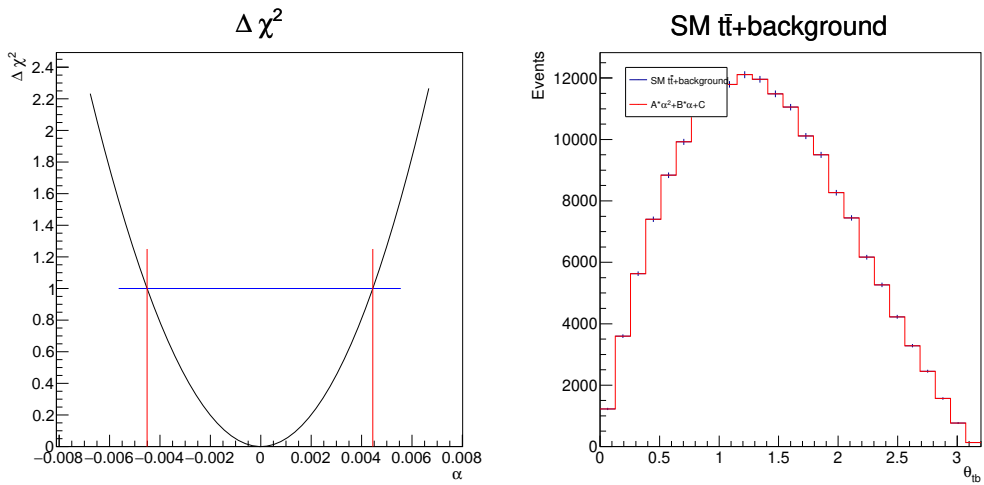
Figure B.2: θ^*_{tb} for vl_tbW_Re.
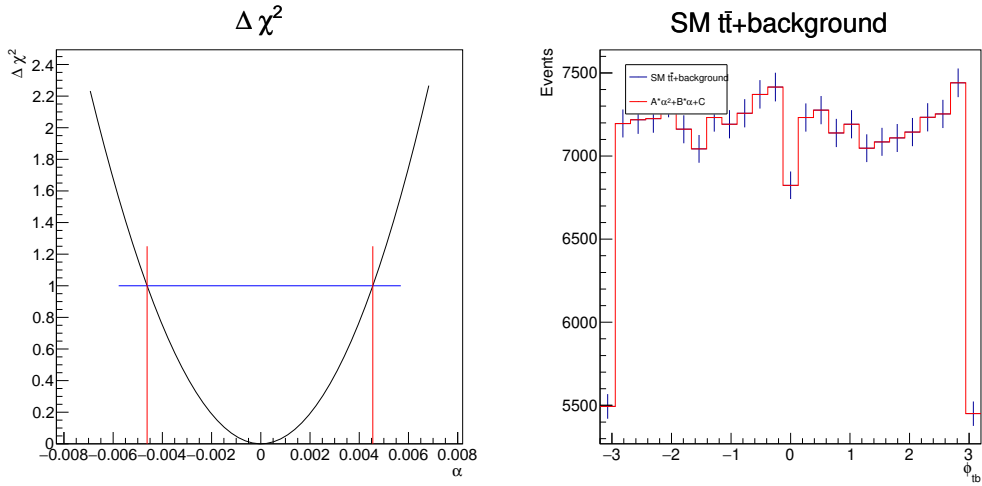
Figure B.3: ϕ_{tb}^* for vl_tbW_Re.
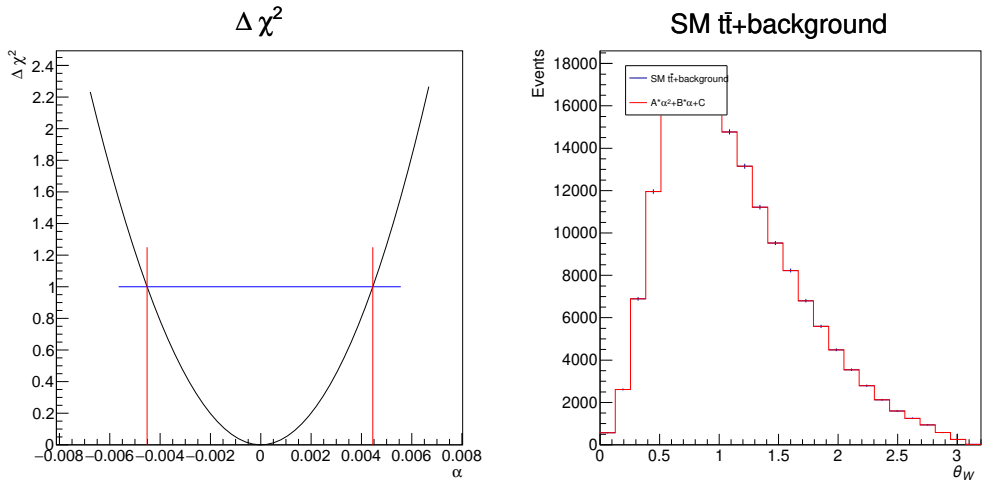
Figure B.4: θ_{Wl}^* for vl_tbW_Re.
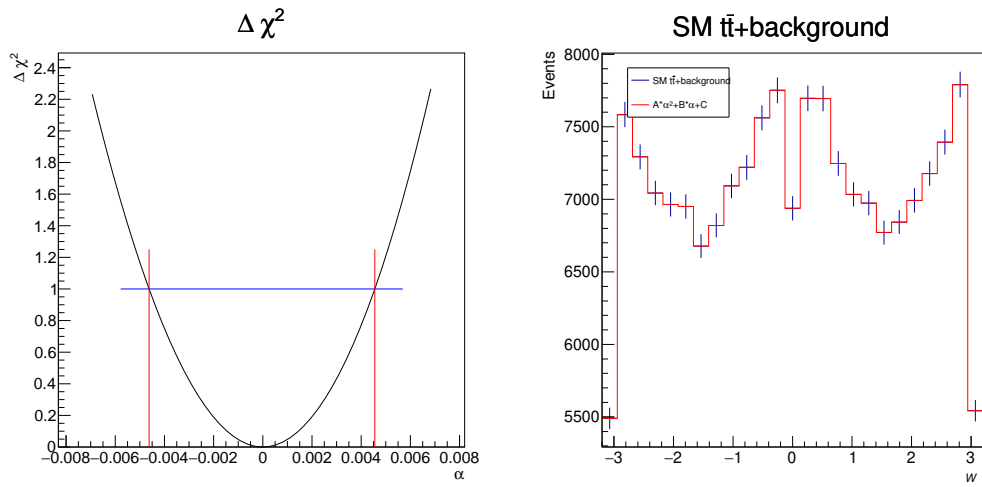
Figure B.5: ϕ_{Wl}^* for vl_tbW_Re.

vr_tbW_Re
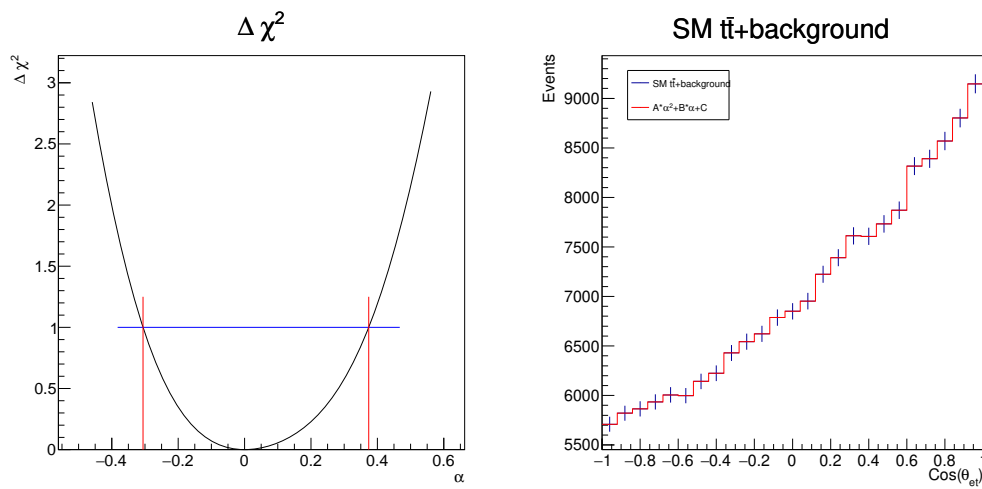
Figure B.6: $\cos\theta_{et}$ for vr_tbW_Re.
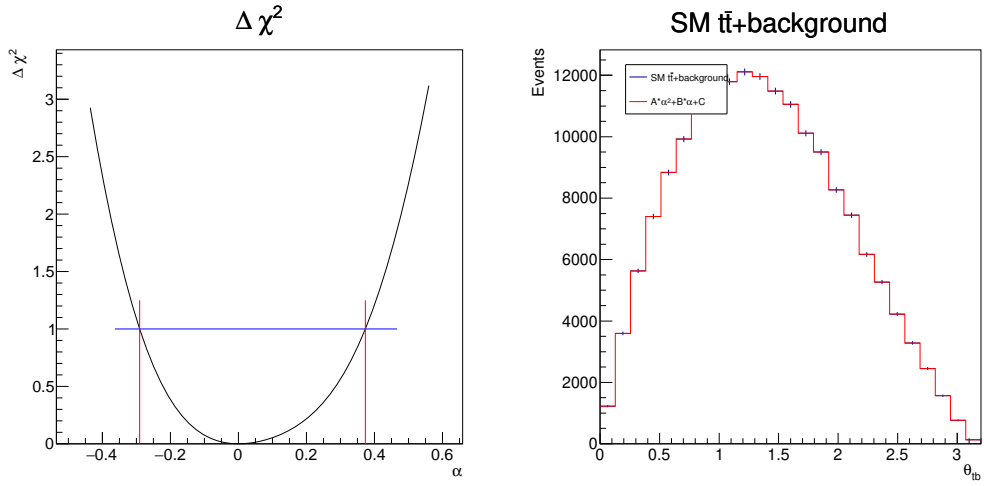
Figure B.7: θ_{tb}^* for vr_tbW_Re.
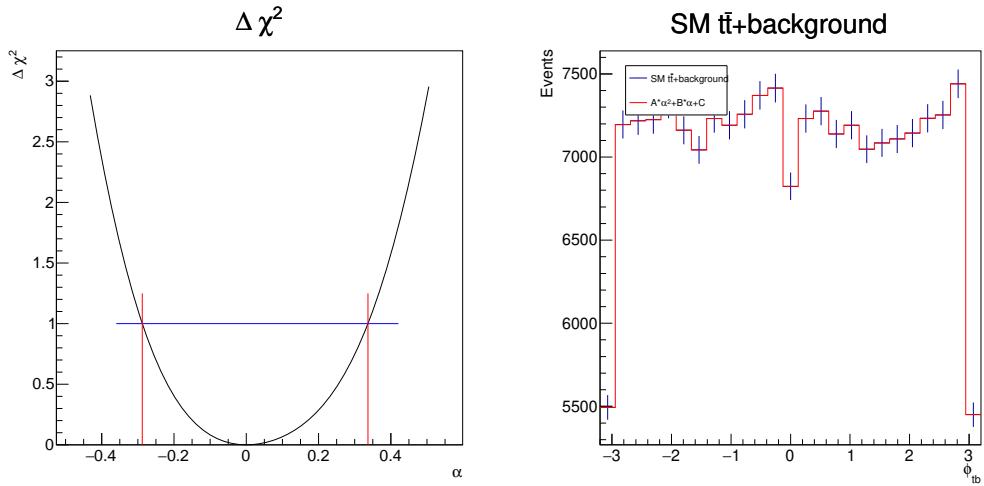
Figure B.8: ϕ_{tb}^* for vr_tbW_Re.
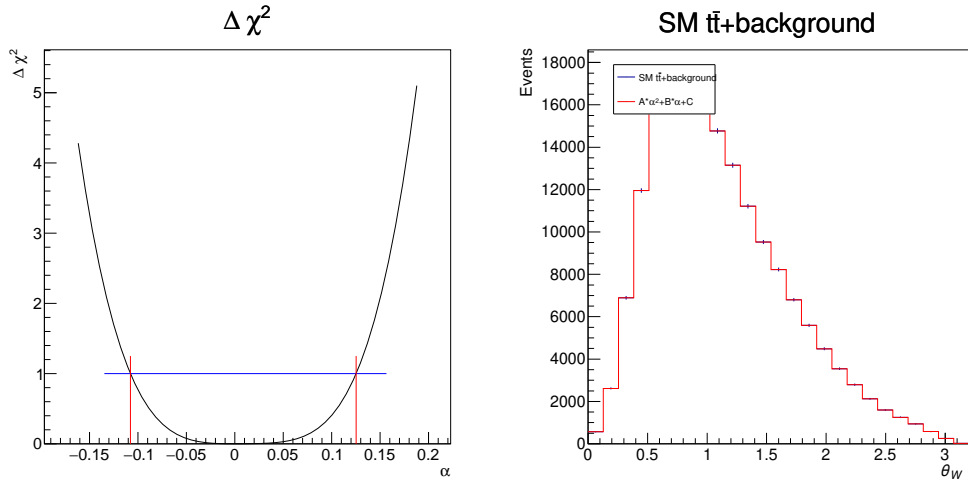
Figure B.9: θ^*_{Wl} for vr_tbW_Re.
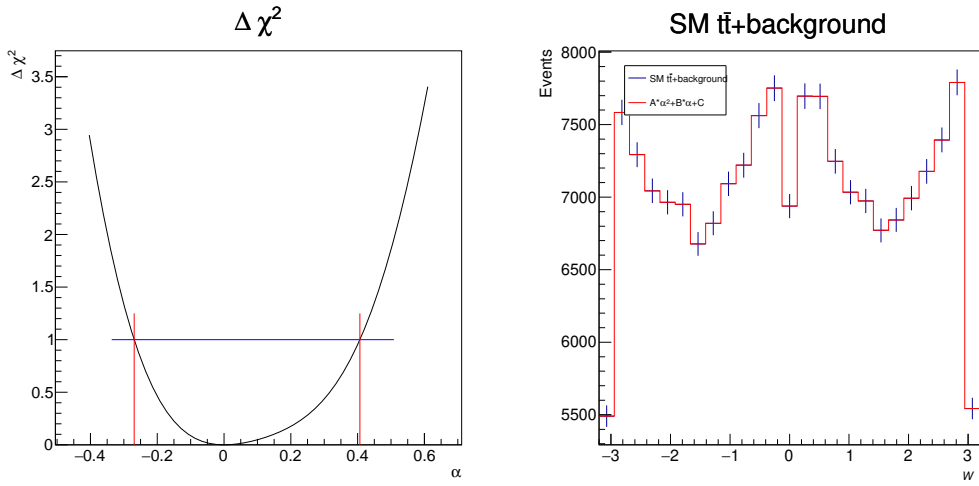
Figure B.10: ϕ^*_{Wl} for vr_tbW_Re.

tl_tbW_Re
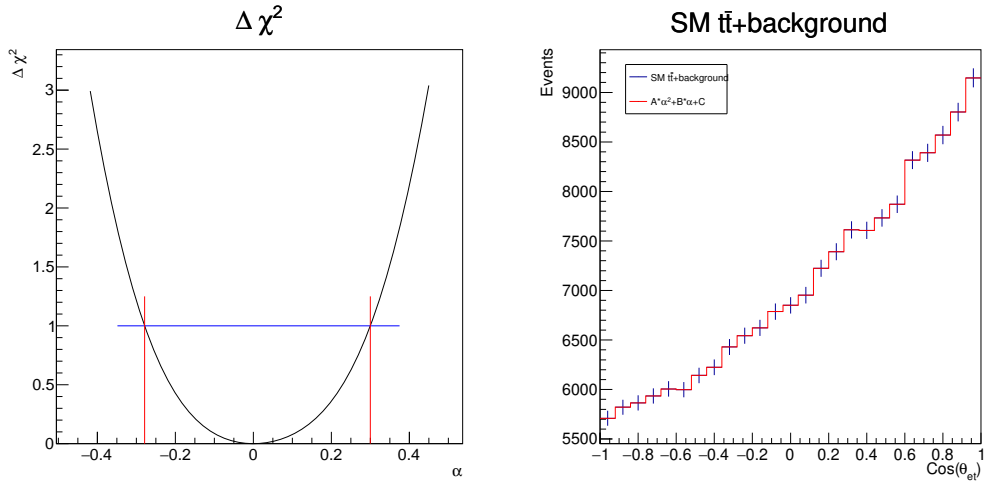
Figure B.11: $\cos\theta_{et}$ for tl_tbW_Re.
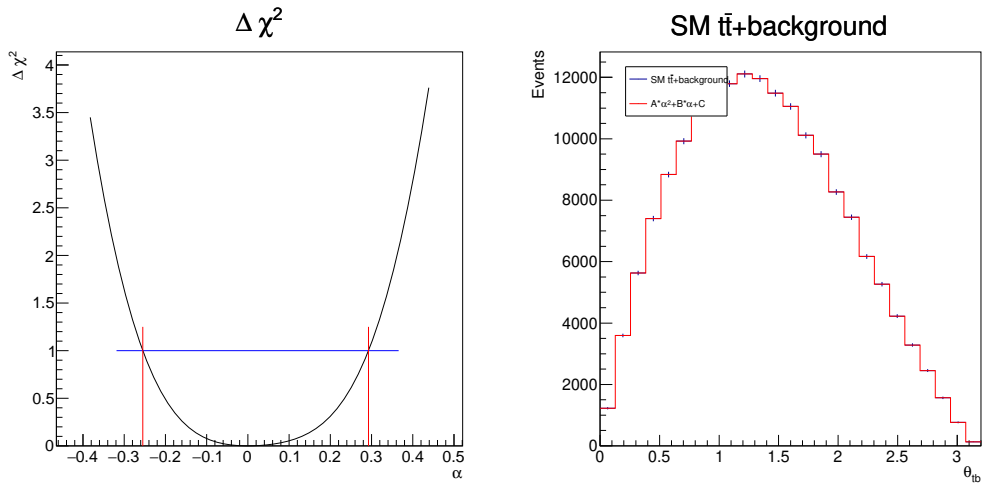
Figure B.12: θ_{tb}^* for tl_tbW_Re.
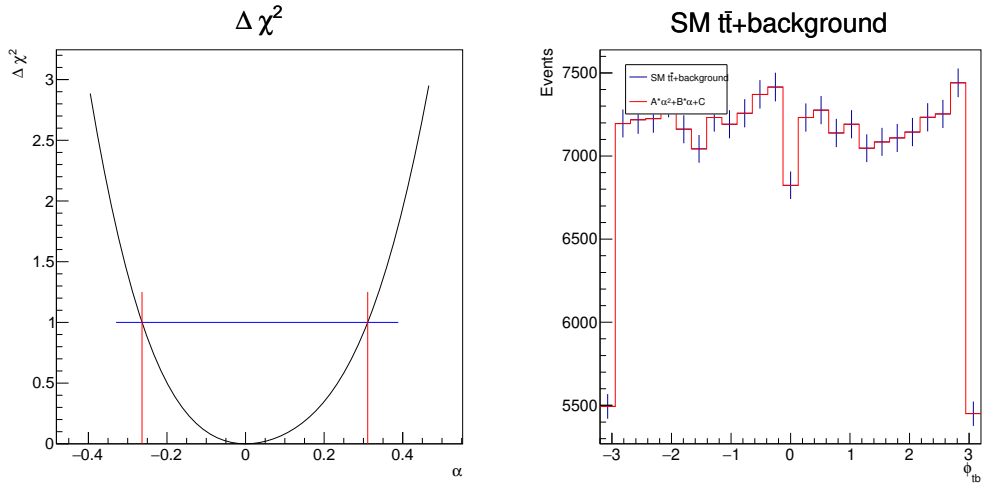
Figure B.13: ϕ_{tb}^* for tl_tbW_Re.
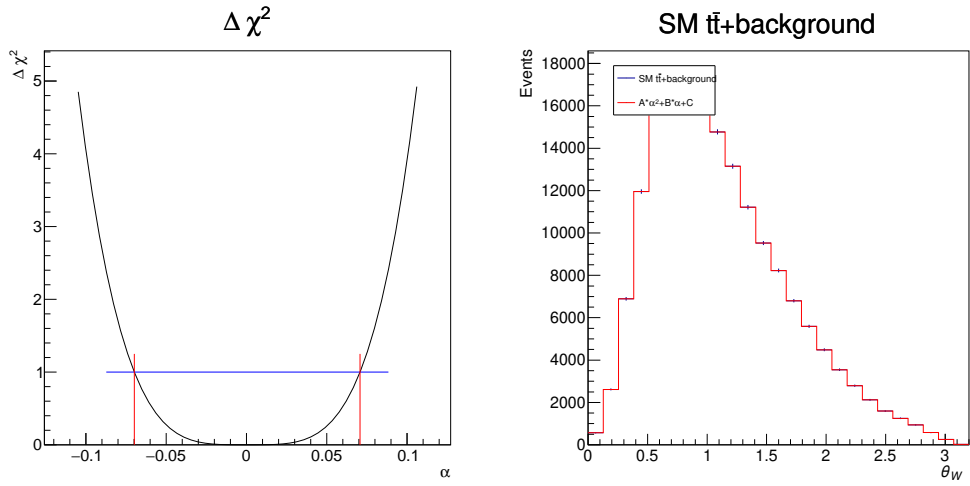
Figure B.14: θ_{Wl}^* for tl_tbW_Re.
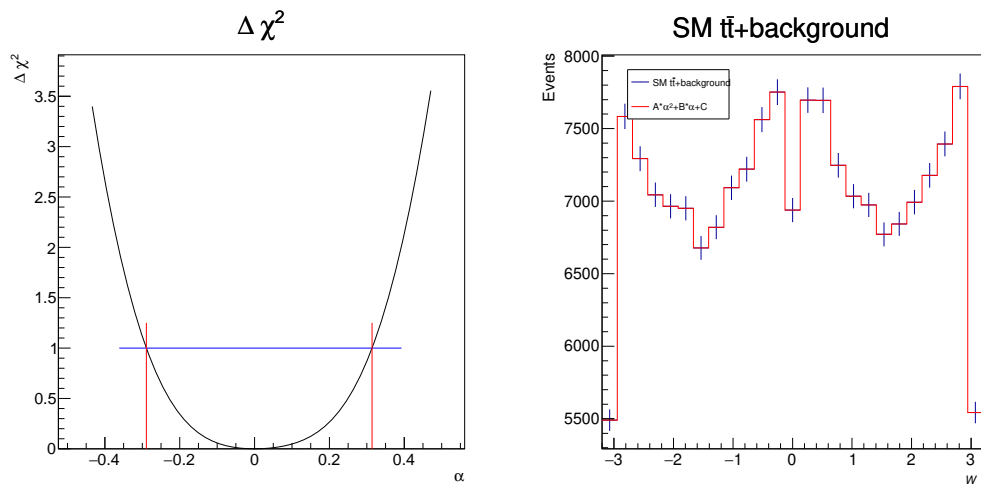
Figure B.15: ϕ_{Wl}^* for tl_tbW_Re.

tr_tbW_Re
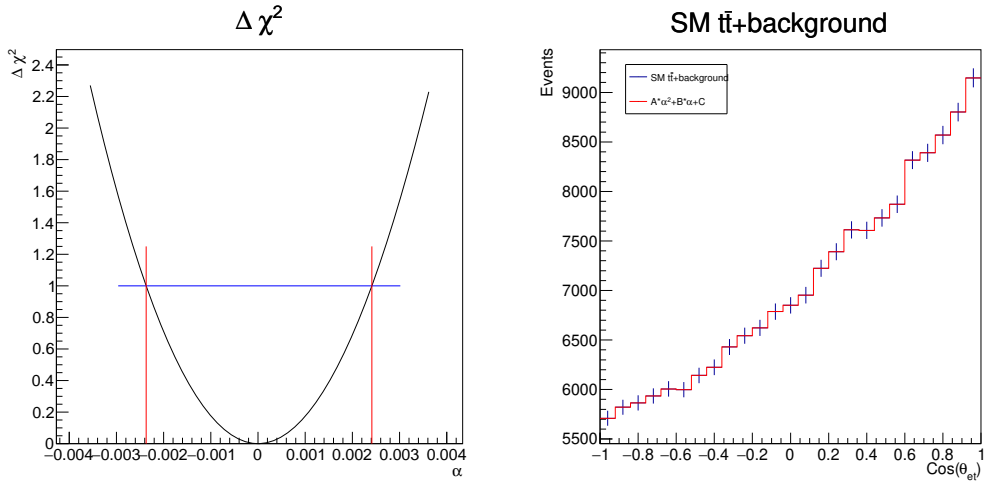
Figure B.16: $\cos\theta_{et}$ for tr_tbW_Re.
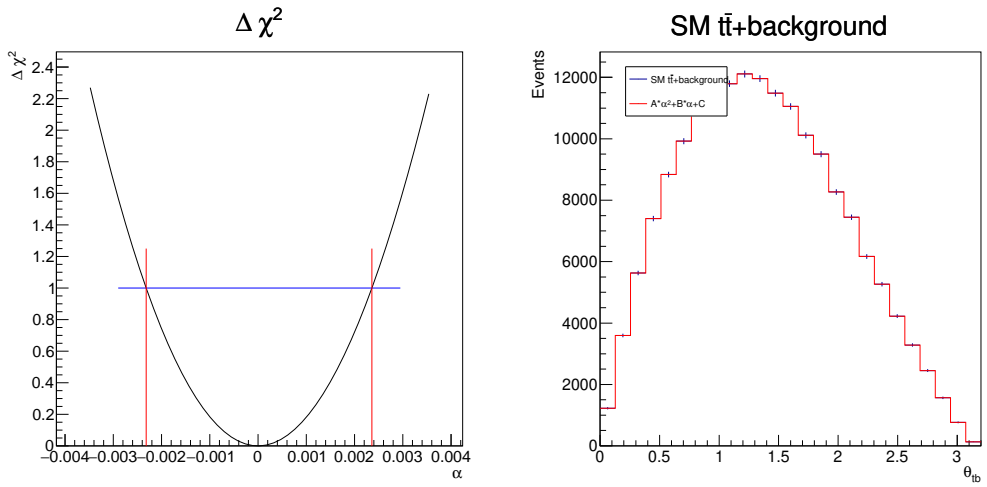
Figure B.17: θ^*_{tb} for tr_tbW_Re.
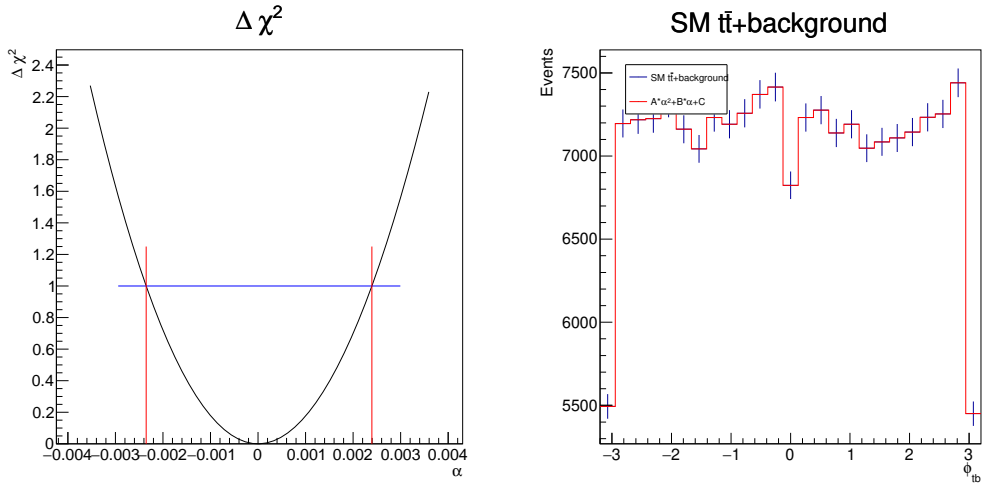
Figure B.18: ϕ_{tb}^* for tr_tbW_Re.
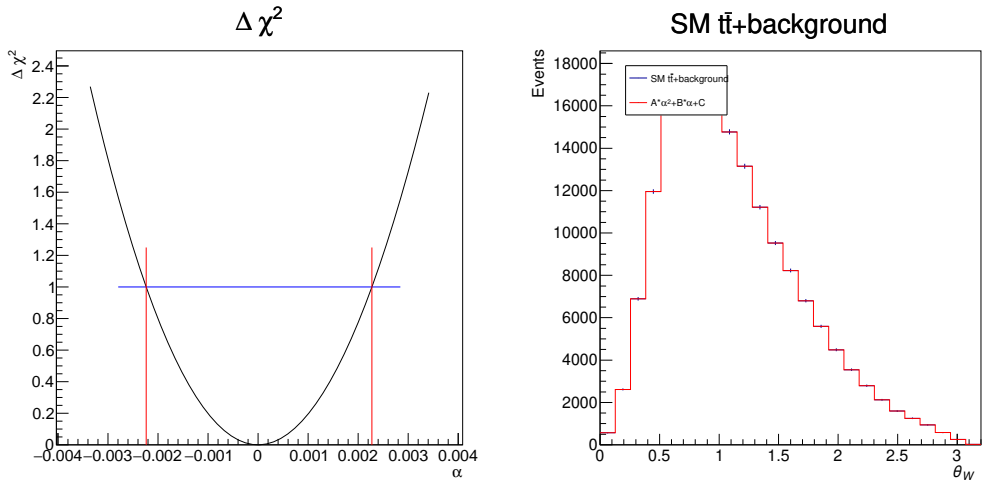
Figure B.19: θ_{Wl}^* for tr_tbW_Re.
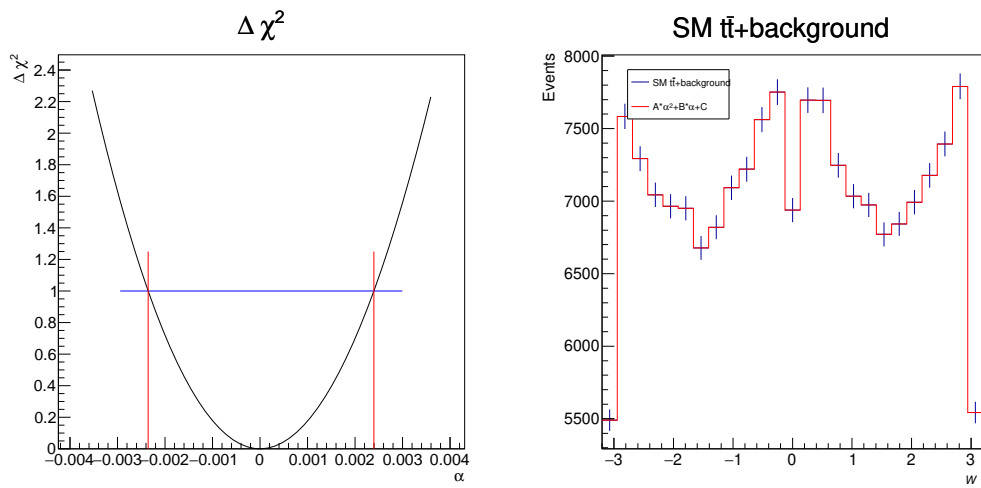
Figure B.20: ϕ_{Wl}^{*} for tr_tbW_Re.

tv_ttA
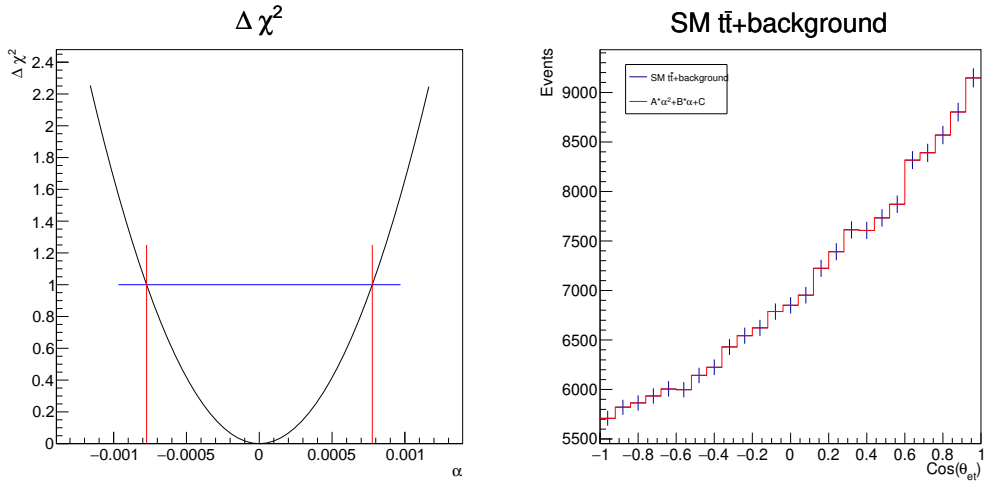
Figure B.21: $\cos\theta_{et}$ for tv_ttA
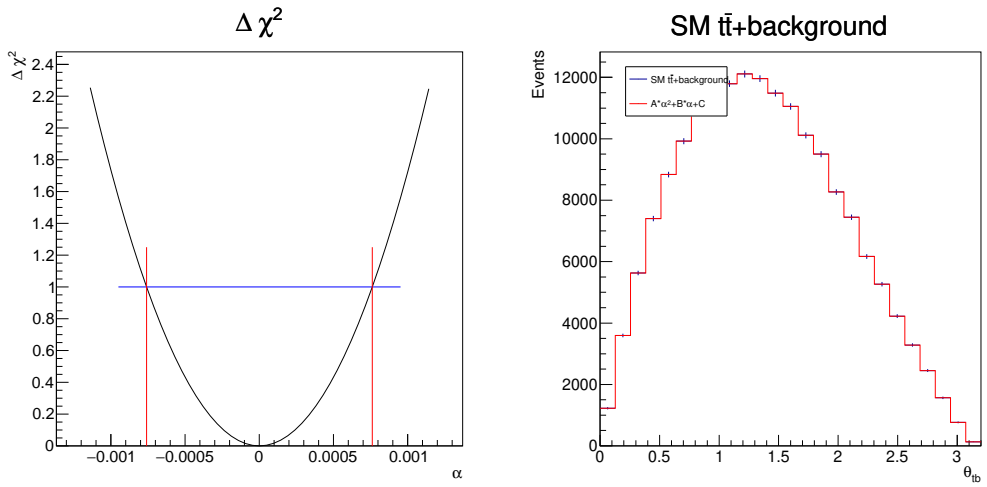
Figure B.22: θ_{tb}^* for tv_ttA
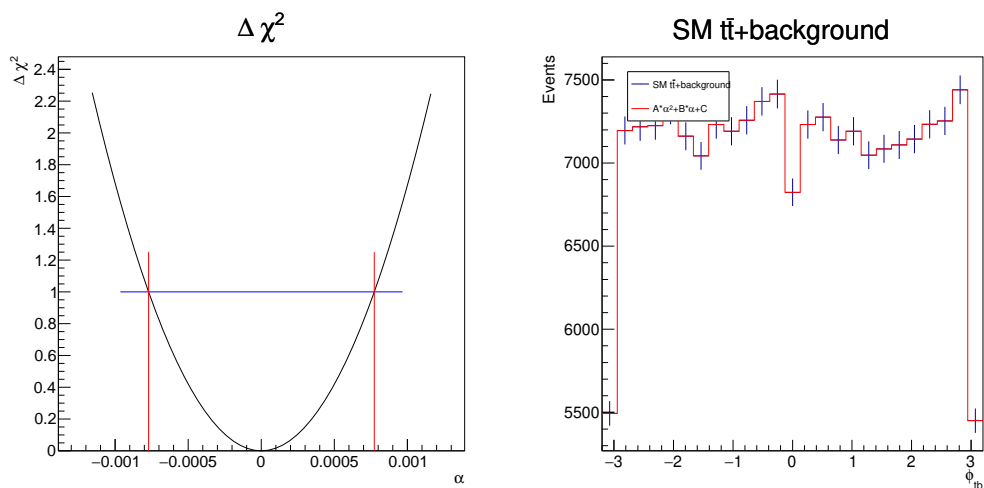
Figure B.23: ϕ_{tb}^* for tv_ttA

Figure B.24: θ_{Wl}^* for tv_ttA

75
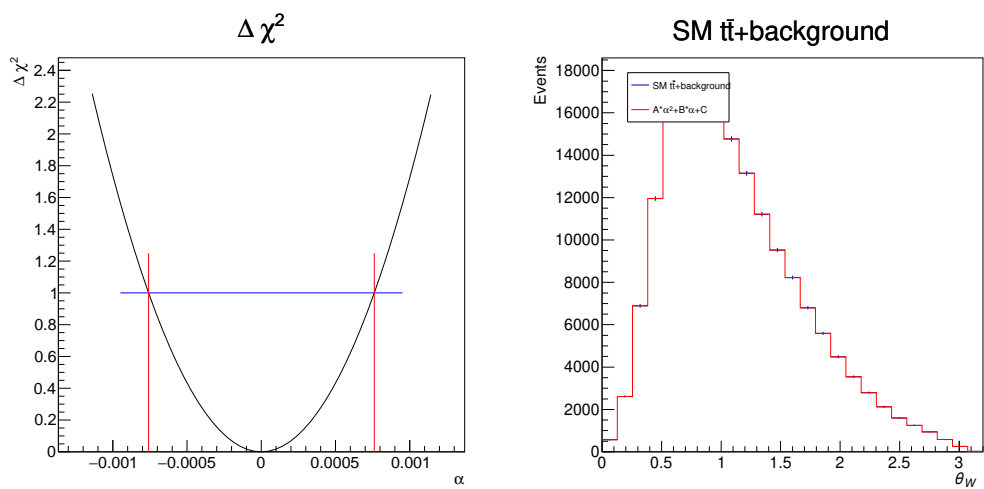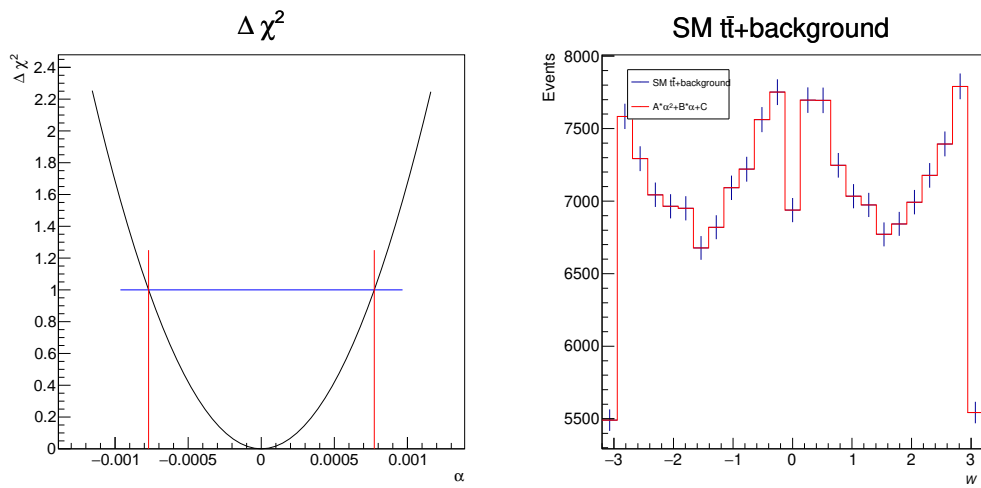
Figure B.25: ϕ_{Wl}^* for tv_ttA
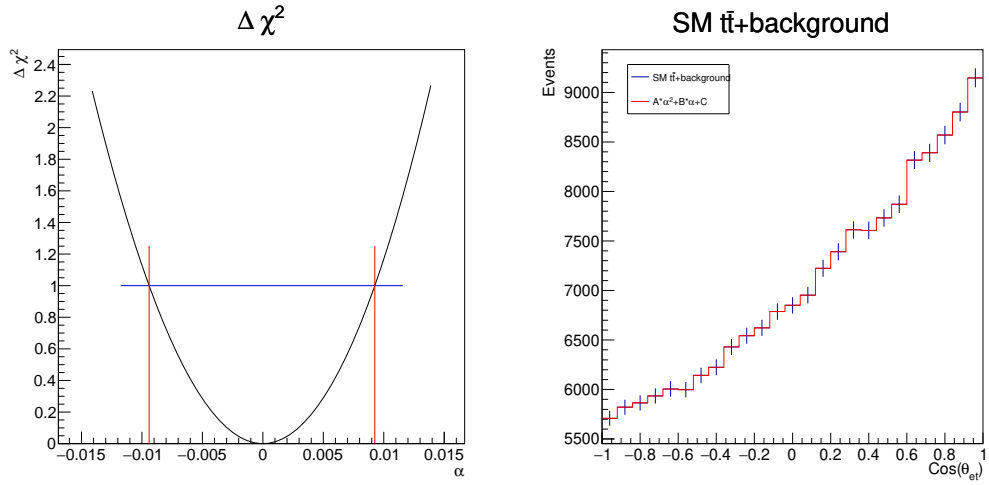
vr_ttZ

Figure B.26: $\cos\theta_{et}$ for vr_ttZ
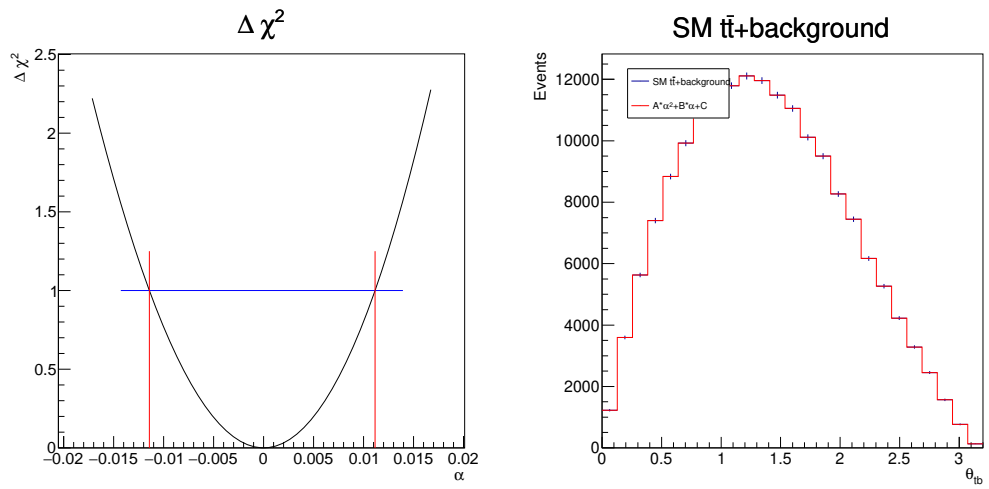
Figure B.27: θ_{tb}^* for vr_ttZ
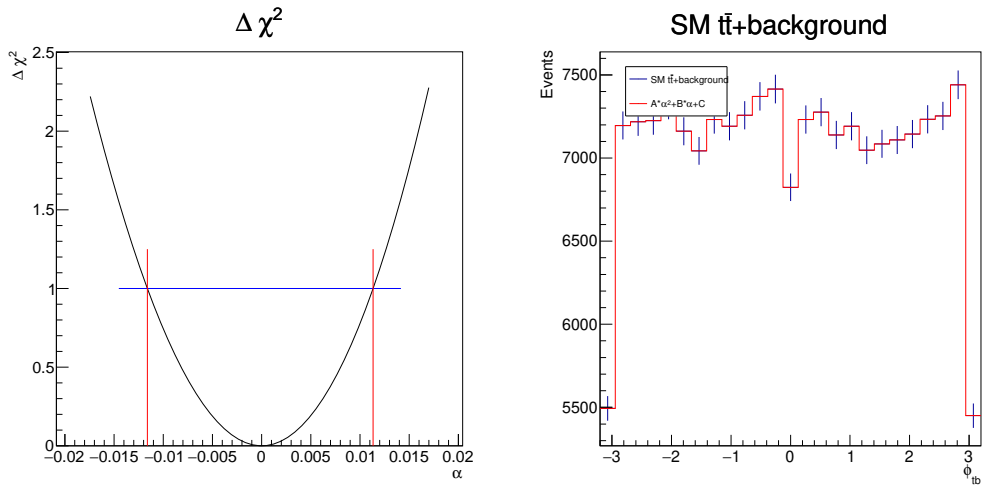
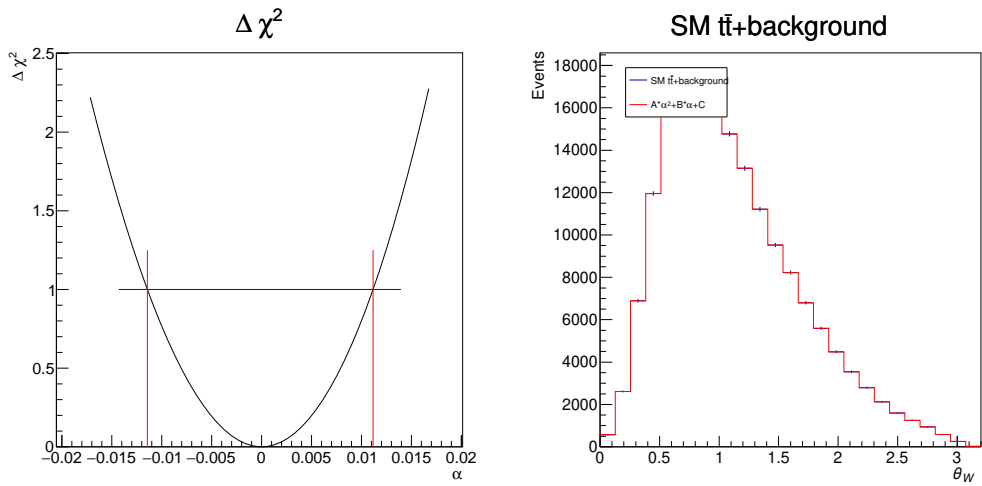Figure B.28: ϕ_{tb}^* for vr_ttZ

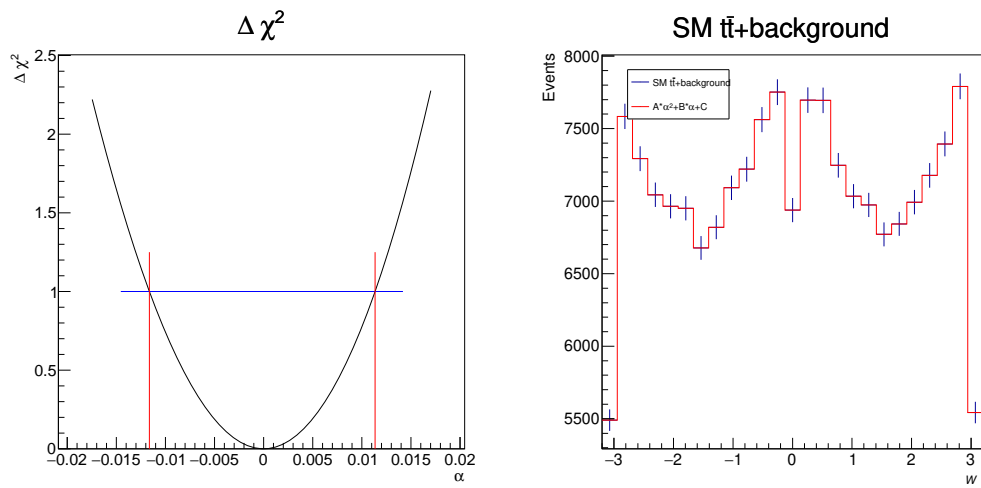Figure B.29: θ_{Wl}^* for vr_ttZ

Figure B.30: ϕ^*_{Wl} for vr_ttZ

References

[1] G. Aad et al. *Observation of a new particle in the search for the Standard Model Higgs boson with the ATLAS detector at the LHC.* Physics Letters B, Volume 716, Issue 1, 2012, Pages 1-29, ISSN 0370-2693, https://doi.org/10.1016/j.physletb.2012.08.020. (https://www.sciencedirect.com/science/article/pii/S037026931200857X).

[2] Particle Data Group and others, Review of Particle Physics, *Progress of Theoretical and Experimental Physics*, Volume 2020, Issue 8, August 2020, 083C01, https://doi.org/10.1093/ptep/ptaa104

[3] Mark Thompson. *Modern Particle Physics.* 2013. Chapters 1, 4, 12, 15, 16 & 17.

[4] F. P. Richard. "Simulations of top quark pair production and kinematics at the FCC-ee". CERN Summer Student Program. CERN. February 2021.

[5] Future Circular Collider Study. Volume 2: The Lepton Collider (FCC-ee) Conceptual Design Report, preprint edited by M. Benedikt et al. CERN accelerator reports, CERN-ACC-2018-0057, Geneva, December 2018. Published in Eur. Phys. J. ST.

[6] Aneesh V. Manohar. "Introduction to Effective Field Theories" (2018). arXiv:1804.05863 [hep-ph].

[7] Grzadkowski, B., Iskrzyński, M., Misiak, M. et al. "Dimension-six terms in the Standard Model Lagrangian". J. High Energ. Phys. 2010, 85 (2010). https://doi.org/10.1007/JHEP10(2010)085

[8] J.A. Aguilar-Saavedra. "A minimal set of top anomalous couplings". Nuclear Physics B, Volume 812, Issues 1–2 (2009), Pages 181-204. ISSN 0550-3213. https://doi.org/10.1016/j.nuclphysb.2008.12.012. (https://www.sciencedirect.com/science/article/pii/S0550321308007062)

[9] G. Roland. "Phenomenological study of anomalous $t - \bar{t}$ production at FCC-ee". Bachelor's Thesis. University of Copenhagen, June 2021.

[10] J. M. Torndal. "A Study of Top Anomalous Couplings at a Future e^+e^- Collider". Master's thesis. University of Copenhagen, August 2021.

[11] Volkl, Valentin et al. *FCCSW.* https://github.com/HEP-FCC/FCCSW/. 2021.

[12] Helsens, Clement et al. *FCCAnalyses*. https://github.com/HEP-FCC/FCCAnalyses/. 2021.

[13] Hansen, Jørgen Beck and Torndal, Julie Munch. *ABCfit++*. https://github.com/Torndal/ABCfitplusplus/. 2021.

[14] G. Ganis, C. Helsens and V. Völkl. "Key4hep, a framework for future HEP experiments and its use in FCC." 2021. https://doi.org/10.48550/arXiv.2111.09874

[15] J. de Favereau et al. "DELPHES 3: a modular framework for fast simulation of a generic collider experiment". In: Journal of High Energy Physics 2014.2 (Feb. 2014). issn: 1029-8479.

[16] W. Kilian, T. Ohl and J. Reuter, "WHIZARD —simulating multi-particle processes at LHC and ILC". The European Physical Journal C. 2011. doi:10.1140/epjc/s10052-011-1742-y. url: https://doi.org/10.1140%2Fepjc%2Fs10052-011-1742-y.

[17] M. Cacciari, G. P. Salam, and G. Soyez. "FastJet user manual". In:The European Physical Journal C 72.3 (Mar. 2012). issn: 1434-6052. doi: 10.1140/epjc/s10052-012-1896-2. url: http://dx.doi.org/10.1140/epjc/s10052-012-1896-2.

[18] Janot, P. Top-quark electroweak couplings at the FCC-ee. J. High Energ. Phys. 2015, 182 (2015). https://doi.org/10.1007/JHEP04(2015)182

[19] M. Shapiro. *Lecture 12: QCD and $e^+e^- \rightarrow$ Hadrons Continued.* Berkeley University, Oct. 2016. url: https://www-atlas.lbl.gov/~shapiro/Physics226/lecture12.pdf.

[20] A. Hocker et al. "TMVA - Toolkit for Multivariate Data Analysis", March 2007. arXiv:physics/0703039.

[21] Volker Blobel. "Least Squares Methods". In: *Formulae and methods in experimental data evaluation, with emphasis on high energy physics v.3 : Articles on statistical and numerical methods.* Vol. 3. CERN, Geneva: The European Physical Society, 1983.

[22] C. Bierlich et al. *A comprehensive guide to the physics and usage of PYTHIA 8.3.* 2022. arXiv:2203.11601 [hep-ph]. https://doi.org/10.48550/arXiv.2203.11601.

[23] V. D. Barger, R. J. N. Phillips (1997) *"Collider Physics"*. Frontier in Physics, Addison-Wesley Publishing Company, Inc.

[24] The Gfitter Group., Haller, J., Hoecker, A. et al. Update of the global electroweak fit and constraints on two-Higgs-doublet models. Eur. Phys. J. C 78, 675 (2018). https://doi.org/10.1140/epjc/s10052-018-6131-3